Development of an Effective Double-Moment Cloud Microphysics Scheme with Prognostic Cloud Condensation Nuclei (CCN) for Weather and Climate Models

KYO-SUN SUNNY LIM AND SONG-YOU HONG

Global Environment Laboratory, Department of Atmospheric Sciences, Yonsei University, Seoul, South Korea

(Manuscript received 10 February 2009, in final form 15 November 2009)

ABSTRACT

A new double-moment bulk cloud microphysics scheme, the Weather Research and Forecasting (WRF) Double-Moment 6-class (WDM6) Microphysics scheme, which is based on the WRF Single-Moment 6-class (WSM6) Microphysics scheme, has been developed. In addition to the prediction for the mixing ratios of six water species (water vapor, cloud droplets, cloud ice, snow, rain, and graupel) in the WSM6 scheme, the number concentrations for cloud and rainwater are also predicted in the WDM6 scheme, together with a prognostic variable of cloud condensation nuclei (CCN) number concentration. The new scheme was evaluated on an idealized 2D thunderstorm test bed. Compared to the simulations from the WSM6 scheme, there are greater differences in the droplet concentration between the convective core and stratiform region in WDM6. The reduction of light precipitation and the increase of moderate precipitation accompanying a marked radar bright band near the freezing level from the WDM6 simulation tend to alleviate existing systematic biases in the case of the WSM6 scheme. The strength of this new microphysics scheme is its ability to allow flexibility in variable raindrop size distribution by predicting the number concentrations of clouds and rain, coupled with the explicit CCN distribution, at a reasonable computational cost.

1. Introduction

In general, there are two distinct approaches to modeling cloud microphysics in atmospheric models: the explicit bin-resolving method and the bulk method. Bin-resolving microphysics models explicitly calculate the particle size distribution and therefore provide more rigorous solutions than bulk models. However, the computational cost associated with bin microphysics remains a restriction for atmospheric models in weather forecasts and climate prediction. Thus, the bulk microphysical parameterization scheme, a relatively simple and computationally efficient approach that predicts several drop size distribution (DSD) moments rather than the DSD itself, has been applied in mesoscale and even some GCM models.

The bulk microphysics scheme can be classified into two different methods: a single-moment approach and a multiple-moment approach. The single-moment bulk microphysical scheme predicts only the mixing ratios of the hydrometeors by representing the hydrometeor size for each class with a distribution function, such as an exponential function or a gamma type (Kessler 1969; Wisner et al. 1972; Lin et al. 1983; Rutledge and Hobbs 1983; Cotton et al. 1986; Dudhia 1989; Tao and Simpson 1993; Walko et al. 1995; Kong and Yau 1997). Meanwhile, the double-moment bulk microphysical scheme predicts not only the mixing ratio of the hydrometeors but also their number concentrations (Ziegler 1985; Murakami 1990; Ikawa and Saito 1991; Wang and Chang 1993; Ferrier 1994; Meyers et al. 1997; Reisner et al. 1998; Cohard and Pinty (2000a, hereafter CP2000; Seifert and Beheng 2001; Morrison et al. 2005; Thompson et al. 2008). Many of the double-moment schemes predict the number concentration for the limited hydrometeor species but not all of them. For example, the Thompson scheme predicts the number concentration only for cloud ice and rain. The number concentration for warm species is diagnosed in Reisner et al. (1998), whereas CP2000 only address double-moment warm-rain microphysics. The cloud number concentration is diagnosed in Morrison et al. (2005) in the public-release version of the Weather Research and Forecasting (WRF).

Corresponding author address: S.-Y. Hong, Dept. of Atmospheric Sciences, Yonsei University, Seoul, South Korea.
E-mail: shong@yonsei.ac.kr

DOI: 10.1175/2009MWR2968.1

The double-moment approach for the bulk microphysics scheme, which allows more flexibility of the size distribution enabling the mean diameter to evolve in contrast to the single-moment approach, has become a promising method to improve the microphysical processes in the mesoscale modeling area; even though it requires more computational time than the single-moment approach. The double-moment microphysics scheme also requires cloud condensation nuclei (CCN) information when the CCN number concentration is predicted. Studies have shown the superiority of the double-moment approach in simulating precipitating convective clouds even though the strength of these double-moment schemes relies on the accuracy of the representation of several microphysical processes (Cohard and Pinty 2000b; Lee et al. 2004; Thompson et al. 2004; Milbrandt and Yau 2005; Phillips et al. 2007; Luo et al. 2008; Morrison et al. 2009). This type of scheme with prognostic equations of the raindrop number concentration is able to produce large drops in a reasonable concentration for a heavily precipitating rainband compared with the single-moment scheme. Cohard and Pinty (2000b) mentioned that an even greater flexibility in bulk microphysical schemes could be offered by considering the time evolution of the cloud droplet concentration through a double-moment approach. Lee et al. (2004) showed empirically that estimating moments of a particle size distribution derived from two given moments is superior to using only a single moment from the data analysis of several convective and stratiform drop size distributions. Morrison et al. (2009) further demonstrated that in an idealized 2D storm experiment, the double-moment scheme enhances the precipitation activities in the trailing stratiform region, whereas the convective activities in the convection core region are weakened because of differences in the rain evaporation rate through variable raindrop size distribution.

The purpose of this study is to develop a new double-moment bulk microphysics parameterization of clouds and precipitation to be applicable in mesoscale and general circulation models. The new scheme is called the WRF double-moment 6-class (WDM6) microphysics scheme because only double-moment warm-rain microphysics, which predicts the number concentration of cloud and rainwater, are added into the corresponding single-moment scheme—that is, the WRF single-moment 6-class (WSM6) scheme (Hong et al. 2004; Hong and Lim 2006). The ice-phase microphysics of Hong et al. (2004) are identical for both the WDM6 and WSM6 schemes. Recognizing the importance of cloud–aerosol interaction in cloud microphysics and radiative properties (Ramanathan et al. 2001; Wang 2005; Khain et al. 2008), a prognostic treatment of CCN particles is introduced for the new scheme to activate cloud waters. An idealized 2D storm test bed is designed to differentiate the simulated storm morphology using the WDM6 and WSM6 schemes along with the intrinsic differences between the two schemes. In addition, CCN the effects on the cloud/raindrop properties and surface precipitation are investigated.

This paper is organized as follows: Section 2 describes the proposed scheme, the numerical experimental setup for the 2D storm test is presented in section 3, and the results are discussed in section 4. The concluding remarks are given in the final section.

2. WDM6 scheme

a. General remarks

The WDM6 scheme is the extended version of the WSM6 because it adds the prognostic number concentration of cloud and rainwater together with the CCN; thus, prognostic water substance variables include water vapor, cloud, rain, ice, snow, and graupel for both the WDM6 and WSM6 schemes. The microphysical properties of the WDM6 scheme are demonstrated in Fig. 1. Each source–sink term in Fig. 1 for the prediction of warm-phases number concentration is described in the appendix, and the list of symbols is provided in Table A1 The "Prevp_rc" term in the green circle in Fig. 1a is responsible for the conversion of raindrops to the cloud droplets based on the study of Khairoutdinov and Kogan (2000).

The formulation of warm-rain processes such as autoconversion and accretion in the WDM6 scheme is based on the studies of CP2000. For other source and sink terms in warm-rain processes, the formulas in the WSM6 scheme were adopted; however, even if the same formula is applied, the terms work differently from the terms in the WSM6 scheme because of the predicted N_C and N_R, which in turn influence the ice processes indirectly.

The cloud–raindrop size distributions in the present scheme are assumed to follow the normalized form and can be expressed as

$$n_X(D_X) = N_X \frac{\alpha_X}{\Gamma(\nu_X)} \lambda_X^{\alpha_X \nu_X} D_X^{\alpha_X \nu_X - 1} \exp[-(\lambda_X D_X)^{\alpha_X}], \tag{1}$$

where the index $X \in [C, R]$ in Eq. (1) represents clouds or rain. Here, λ_X is the corresponding slope parameter, whereas ν_X and α_X are the two dispersion parameters. Also, N_X and D_X represent the predicted total number concentration and diameter of the drop category X, respectively. All microphysical processes in the WDM6

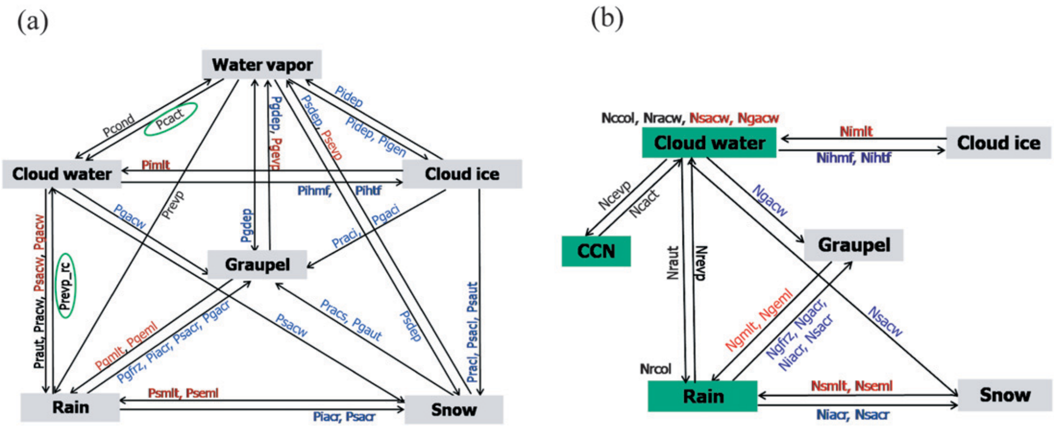

FIG. 1. Flowchart of the microphysics processes for the prediction of (a) the mixing ratios and (b) the number concentrations in the WDM6 scheme. The terms with red (blue) colors are activated when the temperature is above (below) 0°C, whereas the terms with black color are in the entire regime of temperature. The added term compared with the WSM6 scheme is circled in green in (a). Number concentrations of the species in the green box in (b) are only predicted in the current scheme.

scheme are calculated using the particle size distribution from Eq. (1).

The variable slope parameter for X is given by

$$\lambda_X = \left[\frac{\pi}{6}\rho_w \frac{\Gamma(\nu_X + 3/\alpha_X)}{\Gamma(\nu_X)} \frac{N_X}{\rho_a q_X}\right]^{1/3}, \tag{2}$$

where dispersion parameters for the size distribution of rain are chosen as $\nu_R = 2$ and $\alpha_R = 1$, and for the cloud water size distribution ν_C and α_C are chosen as 1 and 3, respectively, based on the report of CP2000. Meanwhile, the WSM6 follows the exponential size distribution for rain, which is represented as

$$n_R(D_R) = N_{0\mathrm{R}} \exp(-\lambda_R D_R). \tag{3}$$

Figure 2 compares the raindrop size distributions represented as Eq. (1) for the WDM6 and as Eq. (3) for the WSM6. The N_R for the WSM6 scheme is not predicted and thus is approximated by the relation of $N_R = N_{0\mathrm{R}}/\lambda_R$. With $N_{0\mathrm{R}}$ ($=8 \times 10^6$ m^{-4}) and q_R ($=1$ g kg^{-1}) in the WSM6 scheme, N_R approximately becomes 3.6×10^3 m^{-3}, which is same to the WDM6 scheme. Thus, the raindrop size distribution with respect to the diameter for the two schemes can be compared as plotted in Fig. 2. The WSM6 scheme shows a monotonic decreasing trend of the number size distribution $n_R(D_R)$ as the diameter of the raindrop increases, whereas the WDM6 scheme shows the maximum diameter size at approximately 300 μm, which decreases at the edge of the diameter range for prescribed N_R and q_R. The gray line in Fig. 2 corresponds to the minimum diameter of the raindrop, 82 μm, where all raindrops are converted into cloud droplets by the evaporation of rain in the WDM6 scheme.

The governing equation of the number concentration for each species is given by

$$\frac{\partial N_X}{\partial t} = -\mathbf{V} \cdot \mathbf{\nabla}_3 N_X - \frac{1}{\rho_a}\frac{\partial}{\partial z}(\rho_a N_X V_X) + S_X, \tag{4}$$

where the first and second terms in the rhs represent the 3D advection and sedimentation for X, respectively. The term S_X represents the source and sink of number concentration for X The number-weighted-mean terminal velocity, which is responsible for the sedimentation of the rain number concentration in Eq. (4), can be obtained by integrating the terminal velocity of rainwater, which is expressed as

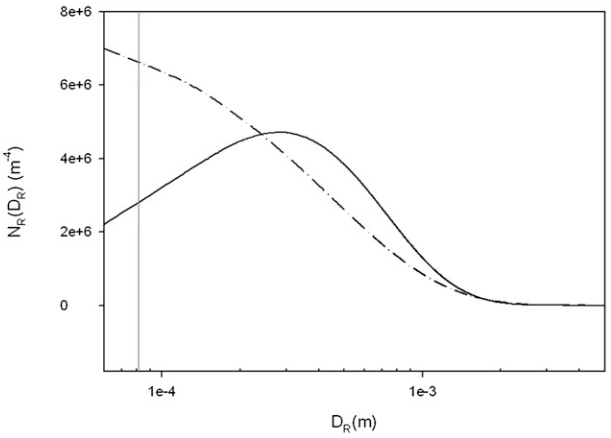

FIG. 2. Raindrop size distribution for the WDM6 (solid) and WSM6 (dashed) physics, with respect to the raindrop diameter. We assumed $\rho_a = 1.0$ kg m^{-3}, $\rho_W = 1000$ kg m^{-3}, $N_R = 3.6 \times 10^3$ m^{-3}, and $q_R = 1.0 \times 10^{-3}$ kg kg^{-1}. The gray line corresponds to 82 μm.

$$\overline{V}_{NR} = \frac{\int V_R(D_R)\,dN_{DR}}{\int dN_{DR}} = \frac{a_R}{\lambda_R^{b_R}}\Gamma(2+b_R)\left(\frac{\rho_0}{\rho_a}\right)^{1/2}, \quad (5)$$

where the terminal velocity $V_R(D_R)$ for a rain particle with diameter D_R is based on the equation determined by Locatelli and Hobbs (1974) and is expressed as

$$V_R(D_R) = a_R D_R^{b_R}\left(\frac{\rho_0}{\rho_a}\right)^{1/2}. \quad (6)$$

b. CCN activation

One of the distinct features in the WDM6 microphysics scheme is that the activated CCN number concentration n_a is predicted and formulated by the drop activation process based on the relationship between the number of activated CCN n_a and supersaturation S_W (Twomey 1959; Khairoutdinov and Kogan 2000), which enables a level of complexity to be added to the traditional bulk microphysics schemes through the explicit CCN cloud-drop concentration feedback. Twomey's relationship between n_a and S_W is represented as $n_a = CS_W^k$. If we define $S_{\max}$ as the supersaturation needed to activate the total particle count $n + N_C$, where n is the total CCN number concentration and N_C is the cloud droplets number concentration, then C can be represented as $C = (n + N_C)S_{\max}^{-k}$. Thus, the number of activated CCN can be expressed as the following:

$$n_a = (n + N_C)\left(\frac{S_w}{S_{\max}}\right)^k, \quad (7)$$

where k is the parameter (=0.6 in this study) following the observation with a typical range from 0.3 to 1.0 (Khairoutdinov and Kogan 2000). An idealized CCN spectrum is used based on the Twomey-type CCN size distribution in Eq. (7), not the detailed trimodal distribution. In the current microphysics scheme, the nucleation process is computed just before the condensation process for the growth of cloud water; the $S_{\max}$ is set to 0.48%. Martin et al. (1994) proposed the $S_{\max}$ of 0.35% ± 0.13% for the continental-type mass. The preliminary results from the present study demonstrated that the simulated results are not sensitive to the magnitude of $S_{\max}$ from 0.22% to 0.8%.

The "Pcact" term in Fig. 1a is responsible for the CCN activation process. Using the relationship of $M_C N_C = \rho_a q_C$, the production rate of the cloud water mixing ratio by the CCN activation can be expressed as

$$\text{Pcact}(\text{kg kg}^{-1}\,\text{s}^{-1}) = \frac{4\pi\rho_W}{3\rho_a}r_{\text{act}}^3 \times \text{Ncact}(\text{m}^{-3}\,\text{s}^{-1}), \quad (8)$$

where r_{act} is the initial radius assumed to be the radius for activated droplets, which is set as 1.5 μm. Khairoutdinov and Kogan (2000) found that the results were relatively insensitive to changes in r_{act} in a range of 1–2 μm. The Ncact represents the generation rate of N_C by the CCN activation process. In addition, the complete evaporation of cloud drops is assumed to return corresponding CCN particles to the total CCN count. Any other CCN sink–source terms, except for the CCN activation and droplet evaporation, are neglected in the WDM6 scheme. The initial value of the CCN number concentration was chosen as 100 cm^{-3} in this study. With the method presented using Eq. (7), the treatment of CCN activation remains the weakest link in the present scheme because this process is derived from a simplified form of the Kohler equation, which requires accurate treatment of the supersaturation. In coarse-resolution simulations, supersaturation is generally not resolved in a grid box; thus, two different regimes addressing the droplet activation process should be taken into account: a high-resolution approach with resolved supersaturation and the relatively large-scale approach with nonresolved supersaturation (Morrison et al. 2005). However, the authors will address this topic in a future study. Further details about the CCN activation process, including the issues in the initial CCN number concentration, are described in the appendix.

c. Autoconversion and accretion processes

Autoconversion parameterization in CP2000 is based on the numerical simulation of the stochastic collection equation suggested by Berry and Reinhardt (1974), which is built on the observation that a characteristic water content L of small drops develops steadily over a characteristic time scale and can be calculated from the τ and expressed as

$$\text{Praut}(\text{kg kg}^{-1}\,\text{s}^{-1}) = \frac{L}{\tau}. \quad (9)$$

These two positive quantities can be expressed as

$$\begin{aligned} L &= 2.7\times 10^{-2}\rho_a q_C\left(\frac{1}{16}\times 10^{20}\sigma_C^3 D_C - 0.4\right) \\ &= 2.7\times 10^{-2}\rho_a q_C\left(\frac{10^{20}}{16\lambda_C^4} - 0.4\right) \quad \text{and} \end{aligned} \quad (9.1)$$

$$\begin{aligned} \tau &= 3.7\frac{1}{\rho_a q_C}(0.5\times 10^6\sigma_C - 7.5)^{-1} \\ &= 3.7\frac{1}{\rho_a q_C}\left(\frac{0.5\times 10^6}{\lambda_C} - 7.5\right)^{-1}. \end{aligned} \quad (9.2)$$

Here, σ_C represents a standard deviation of cloud droplet distribution. For the given cloud conditions, a mean mass

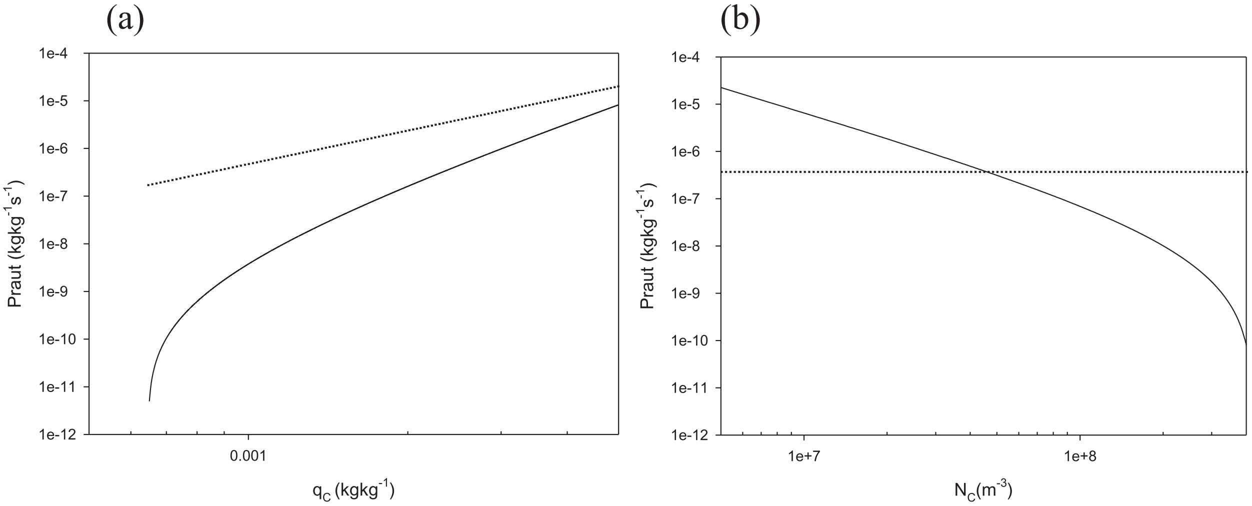

FIG. 3. Production rate of the autoconversion process for the WDM6 (solid) and WSM6 (dotted) physics with respect to (a) cloud water mixing ratios (with assumptions of $N_C = 300$ cm^{-3} and $T = 285$ K) and with respect to (b) cloud water number concentrations (with assumptions of $q_C = 1.0 \times 10^{-3}$ kg kg^{-1} and $T = 285$ K). In the WSM6 scheme, the autoconversion process is activated when q_C is greater than the critical value of q_C. Autoconversion takes place similarly only if $\sigma_C > 15$ μm in the WDM6 scheme. There is no rain generation below 0.65×10^{-3} of q_C in both runs.

autoconversion rate L/τ can be computed only if $\sigma_C >$ 15 μm, whereas sthe WSM6 adopts the autoconversion parameterization suggested by Tripoli and Cotton (1980), which is expressed as Eq. (A38) in Hong and Lim (2006).

In regards to the accretion process, the method of CP2000 obtained by an analytical integration of stochastic collection equation is adopted and expressed as

$$\text{Pracw}(\text{kg kg}^{-1}\,\text{s}^{-1}) = \frac{\pi}{6}\frac{\rho_W}{\rho_a}K_1\frac{N_C N_R}{\lambda_C^3}\left(\frac{2}{\lambda_C^3} + \frac{24}{\lambda_R^3}\right), \quad \text{if} \quad D_R \geq 100\,\mu\text{m}, \quad \text{and} \tag{10.1}$$

$$\text{Pracw}(\text{kg kg}^{-1}\,\text{s}^{-1}) = \frac{\pi}{6}\frac{\rho_W}{\rho_a}K_2\frac{N_C N_R}{\lambda_C^3}\left(\frac{6}{\lambda_C^6} + \frac{5040}{\lambda_R^6}\right), \quad \text{if} \quad D_R < 100\,\mu\text{m}. \tag{10.2}$$

Figure 3 compares the production rates of the autoconversion process between the WDM6 and WSM6 schemes with respect to the cloud water mixing ratio and corresponding number concentration. The rate in the WSM6 shows a more rapid increase than in the WDM6 as the cloud-mixing ratio increases (Fig. 3a). However, the WDM6 scheme shows a rapid conversion rate from existing cloud droplets to rain in the presence of a small number concentration of cloud water (Fig. 3b). The accretion rate obtained from the two different schemes was found to behave very similarly with respect to the mixing ratios and number concentration (data not shown).

Major differences in the warm-rain microphysics between the WDM6 and WSM6 schemes are summarized in Table 1.

d. Computational procedures

In the WDM6 scheme, sedimentation fluxes for both N_R and q_R are computed. Thus, differential settling between drops can be simulated. The sedimentation process of N_R is computed before the source–sink terms. Meanwhile, the sedimentation fluxes of falling N_C are neglected, as in q_c. The freezing–melting processes, which account for the rain and cloud water number concentrations, are considered during the fall-term substeps as in the WSM6 microphysics scheme. The saturation mixing ratios over water and ice are calculated directly, and CCN activation and condensation occur under supersaturated conditions. The CCN activation is computed just before the condensation–evaporation process of cloud water to ensure that any supersaturated water vapor does not pass to the dynamical process.

For other detailed computational procedures refer to Hong and Lim (2006).

3. Numerical experimental setup

The model used in this study is the Advanced Research WRF version 3.0.1 (ARW; Skamarock et al. 2008), which was released in August 2008. The WRF is well suited for a wide range of applications, from idealized research simulations to operational forecasting, and has the flexibility to accommodate future enhancements.

The 2D idealized thunderstorm experiment was designed to systematically distinguish the intrinsic differences between the WDM6 and WSM6 schemes by the virtue of fixed initial conditions and the fact that

TABLE 1. Major differences in warm-rain microphysical properties between the WSM6 and WDM6 schemes.

Properties	Option	Value
Autoconversion	WSM6	$\frac{0.104 g E_C \rho_0^{4/3}}{\mu (N_C \rho_W)^{1/3}} q_C^{7/3} H(q_C - q_{C0})$
	WDM6	L/τ, where $L = 2.7 \times 10^{-2} \rho_a q_C \left(\frac{1}{16} \times 10^{20} \sigma_C^3 D_C - 0.4\right)$ and $\tau = 3.7 \frac{1}{\rho_a q_C} (0.5 \times 10^6 \sigma_C - 7.5)^{-1}$
Accretion	WSM6	$\frac{\pi a_R E_{RC} N_{0R} q_C}{4} \left(\frac{\rho_0}{\rho_a}\right)^{1/2} \frac{\Gamma(3 + b_R)}{\lambda_R^{3+b_R}}$
	WDM6	$\frac{\pi}{6} \frac{\rho_W}{\rho_a} K_1 \frac{N_C N_R}{\lambda_C^3} \left(\frac{2}{\lambda_C^3} + \frac{24}{\lambda_R^3}\right)$, if $D_R \geq 100\,\mu m$ $\frac{\pi}{6} \frac{\rho_W}{\rho_a} K_2 \frac{N_C N_R}{\lambda_C^3} \left(\frac{6}{\lambda_C^6} + \frac{5040}{\lambda_R^6}\right)$, if $D_R < 100\,\mu m$
N_R size distribution	WSM6	$N_R \lambda_R \exp[-(\lambda_R D_R)]$
	WDM6	$N_R \lambda_R^2 D_R \exp[-(\lambda_R D_R)]$
N_C size distribution	WSM6	Constant value with $N_C = 3 \times 10^8$ m^{-3}
	WDM6	$n_C(D_C) = 3 N_C \lambda_C^3 D_C^2 \exp[-(\lambda_C D_C)^3]$

microphysics is the only physical parameterization included. The authors of the present study followed the experimental design of Morrison et al. (2009), which compares storm characteristics. The grid in this direction comprised 601 points with a 1-km grid spacing. The number of vertical layers was 80. The model was integrated for 7 h with a time step of 5 s. The initial condition included a warm bubble with a 4-km radius and a maximum perturbation of 3 K at the center of the domain. A wind with a velocity of 12 m s^{-1} was applied in the positive x direction at the surface; its velocity decreased to zero at 2.5 km above the ground with no wind above. Open boundary conditions were applied and there was no Coriolis force or friction. The only physical parameterization was the microphysics scheme and the other physical processes were turned off, including radiation, vertical diffusion including planetary boundary layer physics, land surface, and deep convection due to the cumulus parameterization scheme.

The Weather Research and Forecasting double-moment and single-moment (WDM and WSM, respectively) experiments with the WDM6 and WSM6 schemes, respectively, were conducted to investigate the overall impact of the double-moment treatment on the simulated storm. In addition to these two experiments, an additional sensitivity experiment, the WARM experiment, was performed to explore fundamental differences between the two schemes (Table 2). In the WARM experiment, all the warm-rain microphysics such as the autoconversion process (Praut) and the accretion process of cloud water by rain (Pracw) in the WDM6 scheme are replaced by the formulae in the WSM6 microphysics scheme. Raindrop size distribution following the normalized form from Eq. (1) is also changed to the exponential form from Eq. (3) (see Table 1). Thus, differences between the WARM and WSM experiments can be attributed to the prognostic versus diagnostic rain number concentrations in microphysics terms. The aerosol effects on the cloud–rain properties and surface precipitation were also investigated by varying the initial CCN number concentration. Because the major purpose of the idealized experiments is to evaluate whether the WDM6 scheme is correctly implemented by comparing the simulated 2D storm structure with the WSM6 scheme and to illuminate the fundamental differences between the two approaches, the discussion will be focused on the differences in the microphysical properties of the simulated storm and associated storm morphology, rather than the interaction between the microphysics and storm dynamics.

4. Results

a. Comparison between the WDM and WSM experiments

The evolution of the storm is shown for each simulation by a time series of maximum/minimum vertical velocities

TABLE 2. Description of experiments conducted in this study.

EXP	Description
WSM	WRF single-moment 6-class microphysics scheme
WDM	WRF double-moment 6-class microphysics scheme
WARM	As in WDM, but with the warm-rain physics and size distribution function for rain in WSM and constant number concentration for water droplets

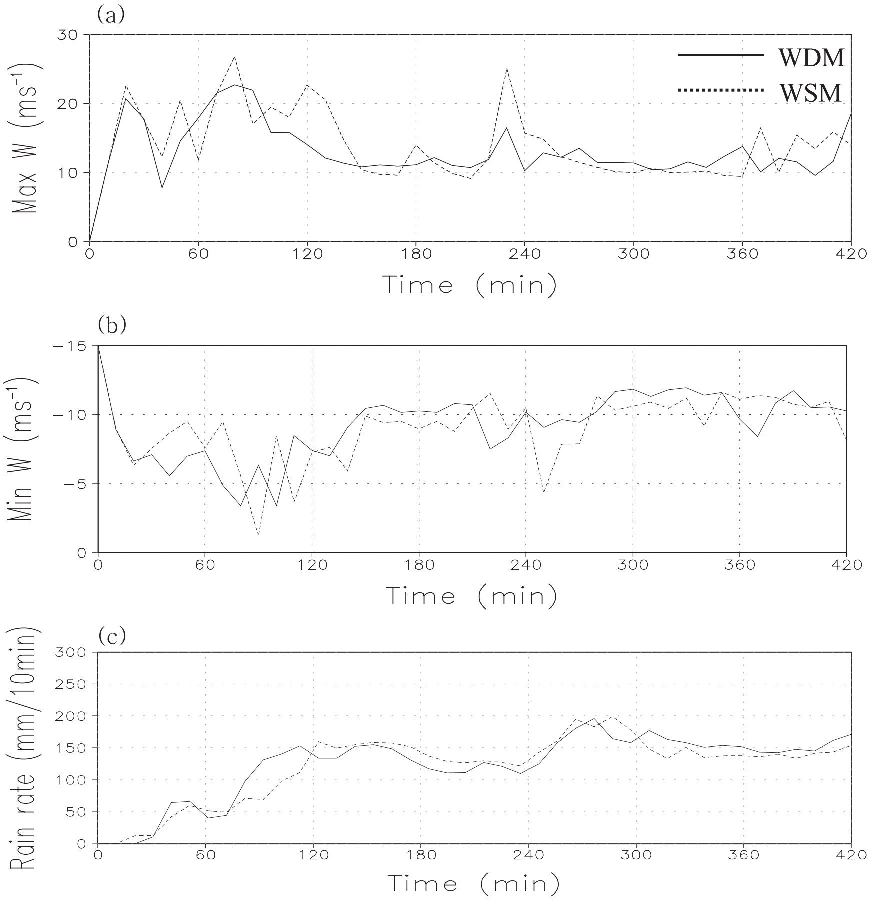

FIG. 4. Time series of (a) maximum vertical velocity, (b) minimum vertical velocity, and (c) the sum of domain-averaged rain rate for the WDM (solid) and WSM (dotted) experiments.

and domain-averaged rain rate in Fig. 4. Updrafts and downdrafts are more transient in terms of peak intensity during the first 2 h of the simulations and another peak is shown at approximately 4 h in both the WDM and WSM experiments, before reaching a mature quasi-equilibrium phase (Figs. 4a,b). For both experiments, the domain-averaged rain rate increases during the initial phase before reaching a quasi-equilibrium state after approximately 5 h of integration, showing the similar trends of surface rainfall (Fig. 4c). Overall, the WDM experiment produces slightly more rain than the WSM during the 7-h integration period (i.e., domain-averaged accumulated amount of precipitation is 8.58 mm in the WDM and 8.39 mm in the WSM).

Figure 5 shows the Hovmöller plots of the surface rainfall rate and maximum vertical reflectivity from the WDM and WSM experiments. Reflectivity was calculated using a simulated equivalent reflectivity factor, which is defined as the sixth moment of the drop size distribution based on the available mixing ratios and number concentrations for precipitation species (rain, snow, and graupel). Bright band (a band of high reflectivity), which is thought to be caused by a liquid skin on melting snow flakes and the enhanced aggregation that occurs among sticky snow flakes, was considered by simply setting the dielectric ratio to 1 in the calculation of equivalent reflectivities for snow and graupel in regions where $T \geq 0°\mathrm{C}$. After 3 h of simulation, areas of light rain rate in the stratiform region are much larger in the WSM run (cf. Figs. 5a,b), even though the domain-averaged precipitation rate is fairly similar between the runs (Fig. 4c). The development of new precipitating cells ahead of the gust front in the established storm's forward environment is visible in both runs with discrete propagation at approximately 4 h of the simulation, which is related to vertically trapped gravity waves (Fovell et al. 2006), as seen in Morrison et al. (2009). Overall, features of the storm evolution are better demonstrated in the maximum reflectivity (Figs. 5c,d). The intensity of the reflectivity is relatively strong in the leading edge in the WDM experiment, whereas in the WSM experiment it is rather uniform from the convection core to the

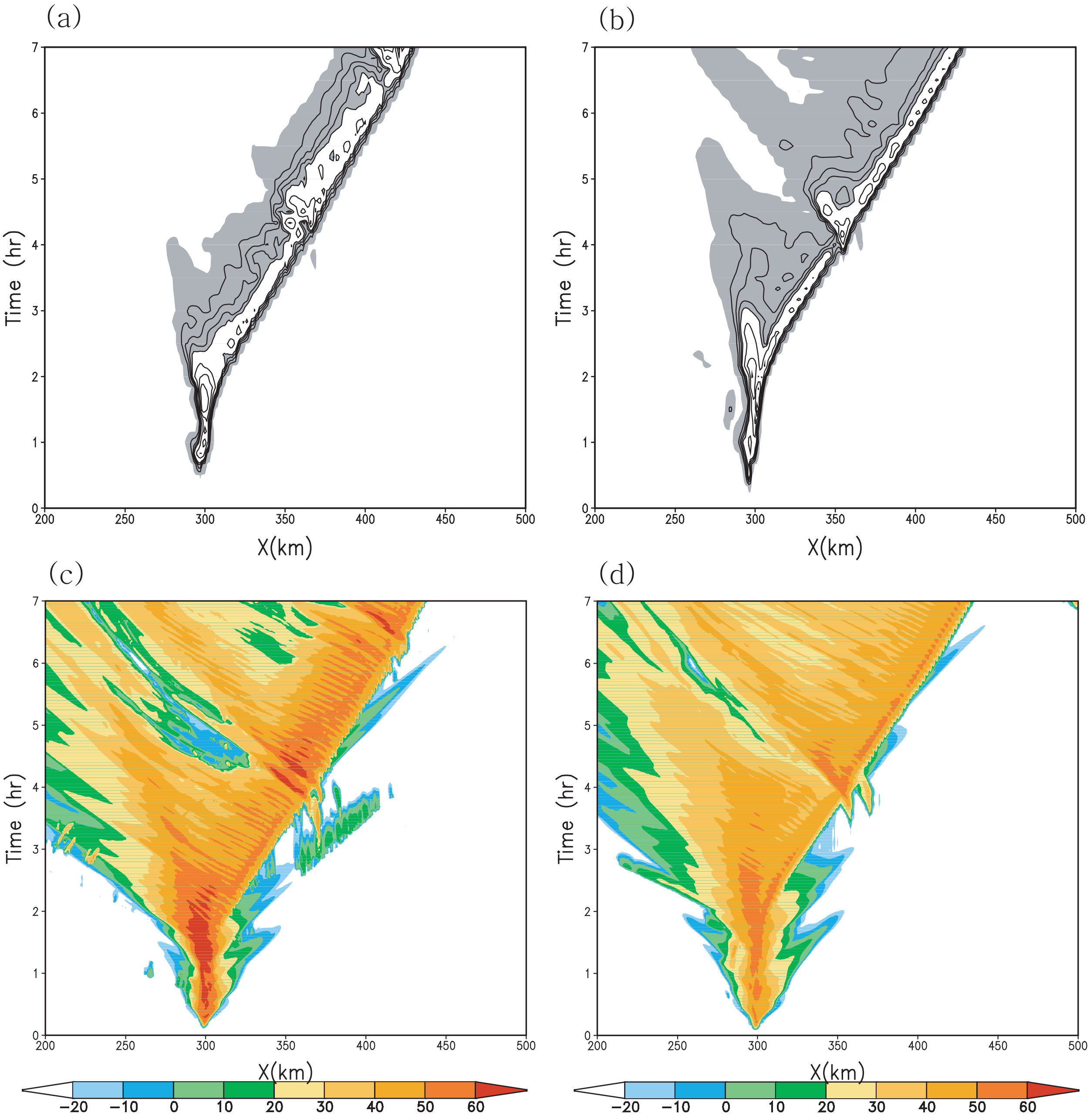

FIG. 5. Hovmöller plots of the surface rainfall rate for the (a) WDM and (b) WSM simulations. The contour interval is every 1 mm (10 min) for rates between 0 and 4 mm (10 min) and every 3 mm (10 min) for rates greater than 4 mm (10 min). To highlight the stratiform rain region, precipitation rates between 0.05 and 4 mm (10 min) are shaded gray. (c),(d) The maximum reflectivity from the WDM and WSM, respectively.

stratiform region. Different evolutions of convective cells between the WDM and WSM runs are further revealed by comparing the snapshots of hydrometeors, with wind vectors and cold pool at 4 and 6 h of the simulation in Fig. 6.

The characteristics of the mesoscale convective system have been evaluated through many observational and modeling studies (Rutledge and MacGorman 1990; Biggerstaff and Houze 1991a,b; Zipser 1977; Bernardet and Cotton 1998; Nagarajan et al. 2004; Li et al. 2009a,b). According to the conceptual model based on observational studies of the kinematic, the thermodynamic structure, and the environmental feature of a convective line with trailing stratiform, the convective upshear-tilted motion is known to begin in the boundary layer near the gust front, extending up through the convection region, and slope more gently into the trailing stratiform cloud

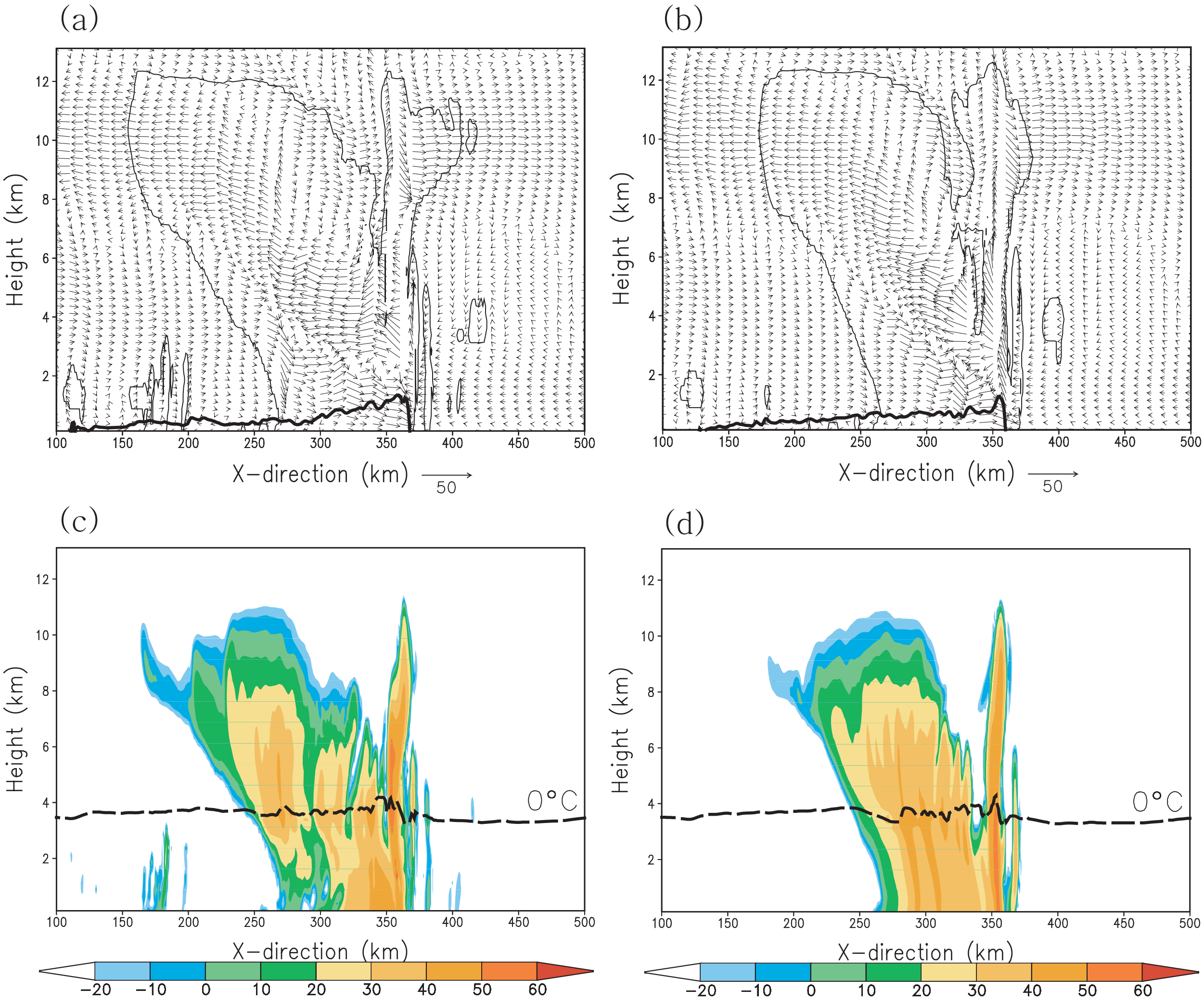

FIG. 6. (a),(b) Storm-relative 2D wind vectors (arrows, m s^{-1}), cold pool defined by the −2 K isotherm of potential temperature perturbation (thick solid line), and boundary of hydrometeors with mixing ratio greater than 0.01 g kg^{-1} (thin solid line) at 4 h. For clarity, the wind vectors are exaggerated by a factor of 5. Only the lowest 13 km of the domain are shown. (c),(d) The simulated reflectivity (dBZ) at 4 h for the two experiments. . The dashed line represents the level of 0°C temperature. (left),(right) The WDM (WSM) simulations.

at middle to upper levels. It should be noted that the kinematic structure of squall lines is typically more complex and often includes a distinct mesoscale updraft at mid- and upper levels as well as a downdraft to the rear of the convective core (Biggerstaff and Houze 1991a).

The previously stated features appear in both simulations at 4 h (Figs. 6a,b). Initiation of convection cells ahead of an existing storm in both runs is responsible for the sharply developed convective cell at approximately 375 km along the x direction in the WDM run and 360 km in the WSM run. The newly initiated convective cells that merged with the oncoming storm further developed into the mesoscale convective system, and the trailing stratiform clouds became separated with new clouds in both runs. Inside of the core convective region, both experiments show strong rainfall intensity of over 50 dBZ with a maximum approximately at 4 km from the surface (cf. Figs. 6c,d). A general trend of downward motion in a current of rear inflow runs under the base of the trailing stratiform region just below the 0°C level, where the radar bright band is relatively distinct in the WDM6 run. The WSM run extends strong reflectivity to the ground level over the stratiform region, as compared to the WDM run. The convection at grid point approximately 175 in the double-moment scheme may be due to a low rain number concentration near the surface, which can enhance the instability near the surface through inefficient evaporation of raindrops, as compared to the value in the single-moment scheme, which results in inefficient evaporation of raindrops (as shown later). The

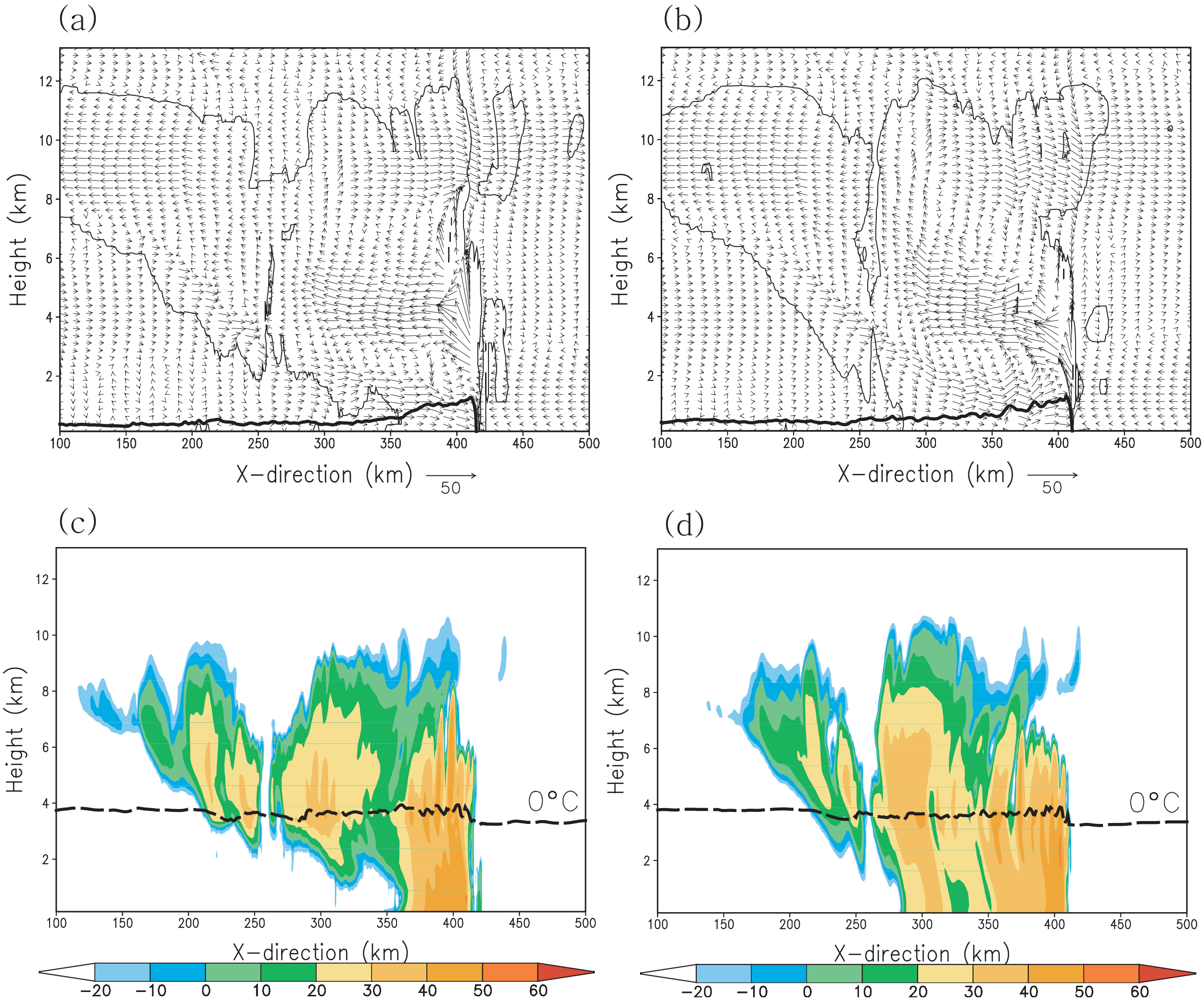

FIG. 7. As in Fig. 6, but at t = 6 h.

separation of the stratiform rain from the convective core is more distinct in the WDM run than in the WSM run, accompanying the weak reflectivity approximately at 300 km. Meanwhile, Li et al. (2009a) demonstrated that cellular convective structures in the form of high-reflectivity cores over the stratiform region, as seen in Figs. 6c,d, were simulated by the bulk microphysics simulation, whereas the stratiform region in the bin simulation is homogeneous with no sign of convective cells embedded.

Low-level downdrafts under the convective core are associated with the heavy rain showers and feed the pool of cold that accumulates below the convective region, whose leading edge is the gust front forming the leading edge of the mesoscale system (Roux 1988; Houze 1993). At 6 h (Fig. 7), a distinct feature observed in the WDM run is the organized downdrafts at 380 km in the x direction with a strengthened cold pool, leading a slightly faster movement of the convective system than the WSM run. This type of rear inflow slantwise circulation over the convective region is weaker and more localized in the WSM run (Figs. 7a,b), which leads to narrower convective precipitation behind the gust front (see Figs. 5a,b). Meanwhile, the horizontal extent of the storm accompanying surface precipitation is broader in the WSM run than in the WDM run.

Analysis of the radar reflectivity reveals a clear difference in the storm morphology (Figs. 7c,d). A large stratiform area develops from older cells blending together as the cells begin to weaken. Each convective element goes through a life cycle, which at the end weakens and becomes a component of a region of stratiform precipitation falling from the midlevel base of the general stratiform cloud shield, in agreement with the study of

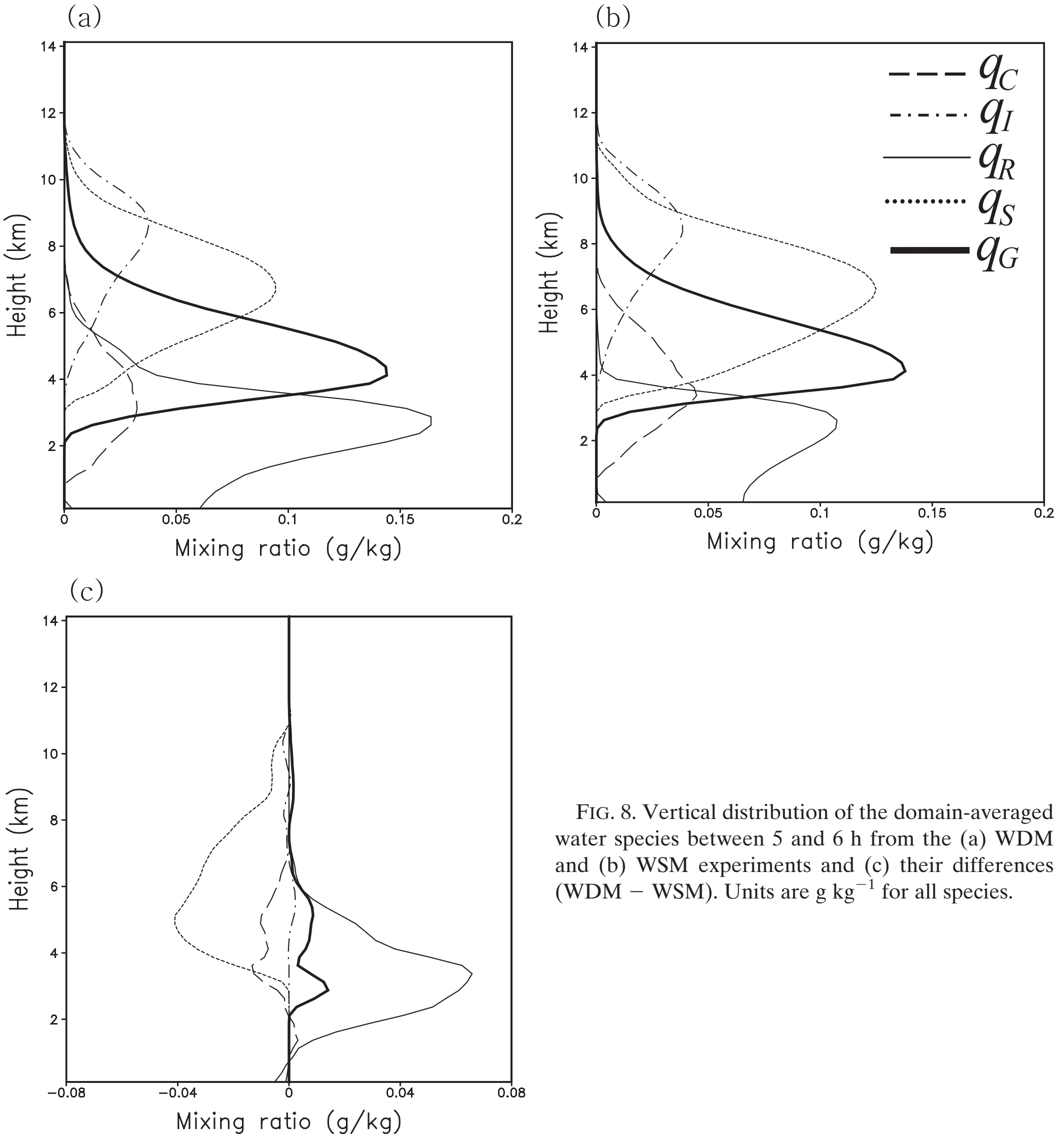

FIG. 8. Vertical distribution of the domain-averaged water species between 5 and 6 h from the (a) WDM and (b) WSM experiments and (c) their differences (WDM − WSM). Units are g kg^{-1} for all species.

Leary and Houze (1979). When several neighboring cells reach this stage, the cells may become indistinguishable from each other, and together they can form an extensive region of stratiform rain with a continuous melting layer. The relatively extensive area of stratiform rain in the WSM run results from the smaller rain number concentrations, which fall faster to reach the ground than in the WDM run. The WDM run shows significantly less precipitation near the surface over the corresponding region, indicating an enhanced evaporation of raindrops.

The vertical profiles of the domain-averaged condensates obtained from the WDM and WSM experiments and their differences are plotted in Fig. 8. Both experiments produce similar profiles of ice phases such as ice, snow, and graupel (Figs. 8a,b) because the WDM6 scheme follows the cold-rain process of the WSM6 scheme and the added processes in the WDM6 scheme do not affect the ice-phases properties directly. The increase of the rainwater mixing ratio below 5 km with less cloud droplet mixing ratio is pronounced when the WDM6 scheme is used (Fig. 8c). The increase of rainwater above the freezing level in the case of the WDM run would reflect an active conversion of cloud droplets to rain when the cloud number concentration is low (see Fig. 3b). Decreased snow in the middle troposphere can be deduced from the ineffective conversion from cloud ice to snow, rather than to graupel through the accretion process of cloud ice by rain (Praci).

To further illustrate the reason for abundant raindrops in the middle lower troposphere in the case of the

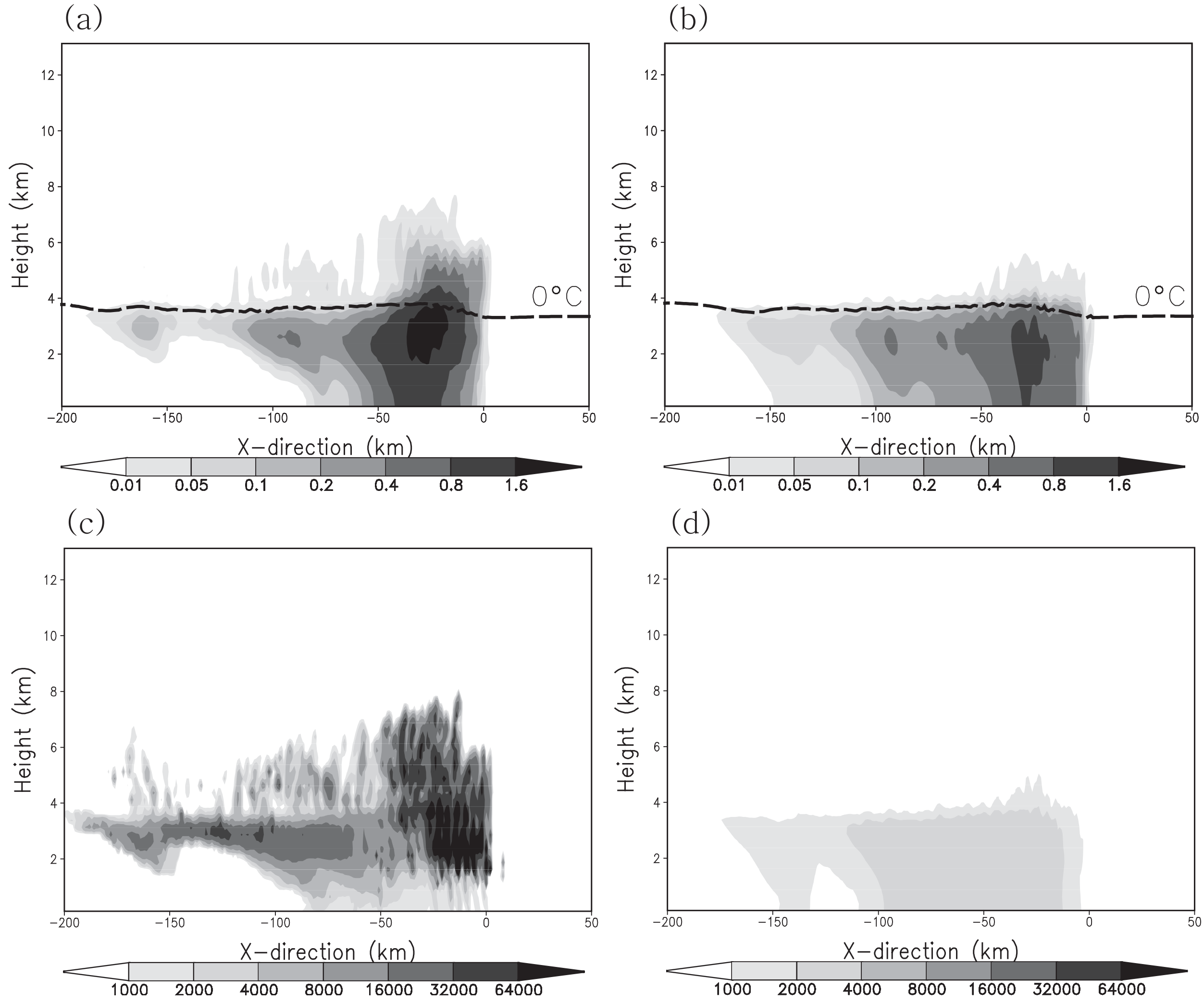

FIG. 9. Rain mixing ratio (g kg^{-1}) averaged between 5 and 6 h as a function of the relative distance from the leading edge of precipitation from the (a) WDM and (b) WSM experiments and rain number concentration (m^{-3}) averaged between 5 and 6 h as a prognostic variable in the (c) WDM experiment and as a diagnosed variable, which is calculated using the slope of the rain size distribution and intercept parameter of rain in the WSM6 microphysics scheme, in the (d) WSM experiment.

WDM6 physics, the averaged mixing ratios between 5 and 6 h in Figs. 9a,b were examined after the simulations have attained quasiequilibrium. In both runs, the amount of rainwater is localized over the convective core region but with more trailing stratiform rain reaching the surface in the WSM experiment. The magnitude of the mixing ratio in the convective core region from the WDM run is approximately doubled, compared with that from the WSM run. The WDM run produces rainwater above the melting layer in the stratiform region, which is not shown in the WSM run. Skofronick-Jackson et al. (2003) showed that the rain content can exist above the 0°C level over the quasi-stratiform cloud region from the airborne active and wideband (10–240 GHz) passive observation. Rain number concentrations N_R with the 2 different microphysics schemes as a prognostic variable in the WDM and a diagnosed variable in the WSM are also presented in Figs. 9c,d. The WDM6 physics show larger N_R except for the lower level near the surface as compared to the WSM6 physics, which has a rather uniform distribution in the vertical direction and a significantly smaller N_R overall. The WDM run also produces more N_R over the convective core region than in the trailing stratiform region. The subject of N_R will be further discussed in the later part of this section. Along the bright band below the freezing level that was identified by previous studies (e.g., Biggerstaff and Houze 1991a,b), the WDM run produces abundant raindrops, which hang over the melting layer but do not fall to the ground. Penetration of N_R and q_R above the melting

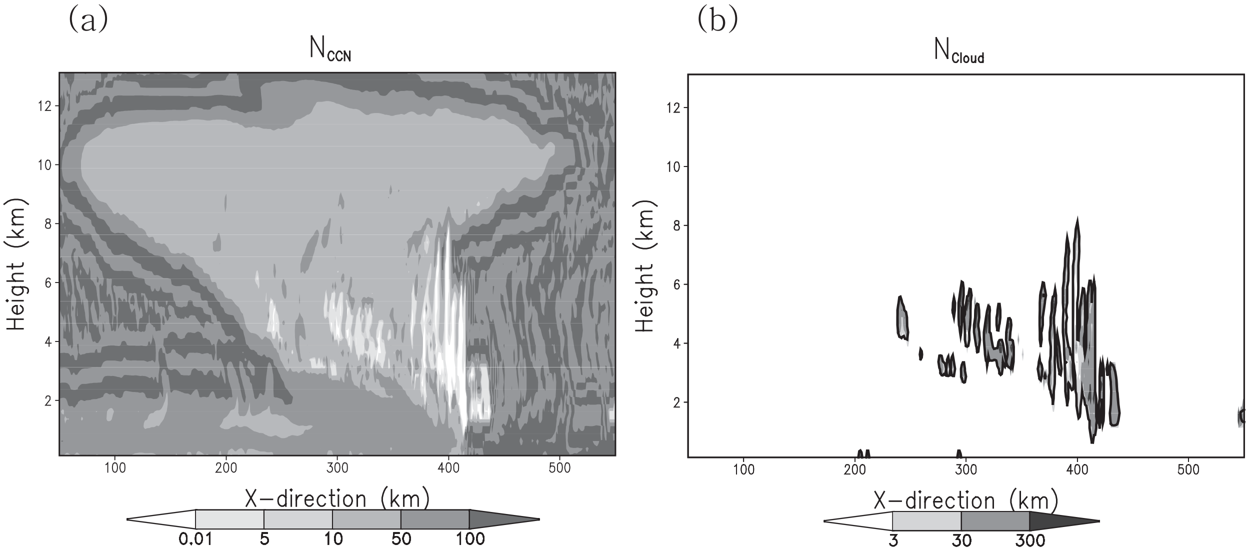

FIG. 10. Simulated number concentrations (cm^{-3}) of the (a) CCN and (b) cloud water, obtained from the WDM experiment at 6 h. Cloud water mixing ratio corresponding to 0.01 g kg^{-1} is also represented in (b) with black contours.

layer, which can be caused by either local production of autoconversion or transport from below the melting level, is prominent in the WDM run. These characteristics are less distinct with an ambiguous boundary of the convective and stratiform region in the WSM run.

A close inspection reveals the melting processes of snow and graupel (Nsmlt, Nseml, Ngmlt, and Ngeml) are the main source terms for the rain number concentration at the melting level, with significantly higher rain number concentration in the WDM run. This increase in N_R induces the raindrops to fall slower with the increase of mass below the melting layer, which is why intense reflectivity appears over the melting layer (3–5 km). Consequently, the enhanced evaporation of raindrops due to high N_R results in the significant reduction of precipitation reaching the surface. This point will be further addressed in the sensitivity experiment.

Figure 10 shows the simulated number concentration of CCN and cloud water in the WDM run. Notably, most CCN are activated over the convective core region, where an abundant amount of cloud droplets are generated. The reduction of the CCN is pronounced inside the storm and at lower levels behind the passage of the storm. The alternating banded pattern of CCN fields outside of a cloud shown in Fig. 10a seems to be due to the propagation of a gravity wave originating from a strong convection. The alternating updrafts and downdrafts were analyzed outside a storm (not shown). The activation of the CCN along the updrafts (supersaturation) and its generation along the downdraft regions (subsaturation) could produce such banded patterns. The CCN of less than 0.01 cm^{-3} applies to the area of cloud number concentration greater than 3 cm^{-3}, whereas its magnitude is much less than in the WSM run, in which the cloud water number concentration is prescribed as a constant value of 300 cm^{-3}. The predicted number concentration of cloud droplets in the WDM experiment was found to follow the distribution of cloud water (Fig. 10b).

A direct comparison of the magnitude of the cloud number concentration between the WDM and WSM runs is less meaningful because the CCN interacts explicitly with cloud droplets in the WDM6 scheme. Additionally, the magnitude of CCN and cloud water number concentrations in the WDM6 scheme cannot be justified in this paper, although the prognostic CCN is correctly coupled with the hydrometeors in association with the characteristics of the storm. Preliminary sensitivity results also showed that the increase of initial CCN tends to increase cloud number concentrations and decrease rain number concentrations, reflecting the cloud–aerosol interaction revealed by previous studies (Ramanathan et al. 2001; Wang 2005; Khain et al. 2008). Responses of the cloud properties, including the cloud number concentration and mean volume diameter with the CCN number concentration, will be discussed in section 4b in detail.

Figure 11 shows the storm characteristics from the WARM experiment. As expected, the storm morphology from the WARM experiment has characteristics of both the WDM6 in terms of overall morphology and the WSM6 in terms of detailed structures. The Hovmöller plot for rain rate in the WARM experiment largely follows the evolutionary feature from the WDM experiment but with a weakened intensity of rain rate over the

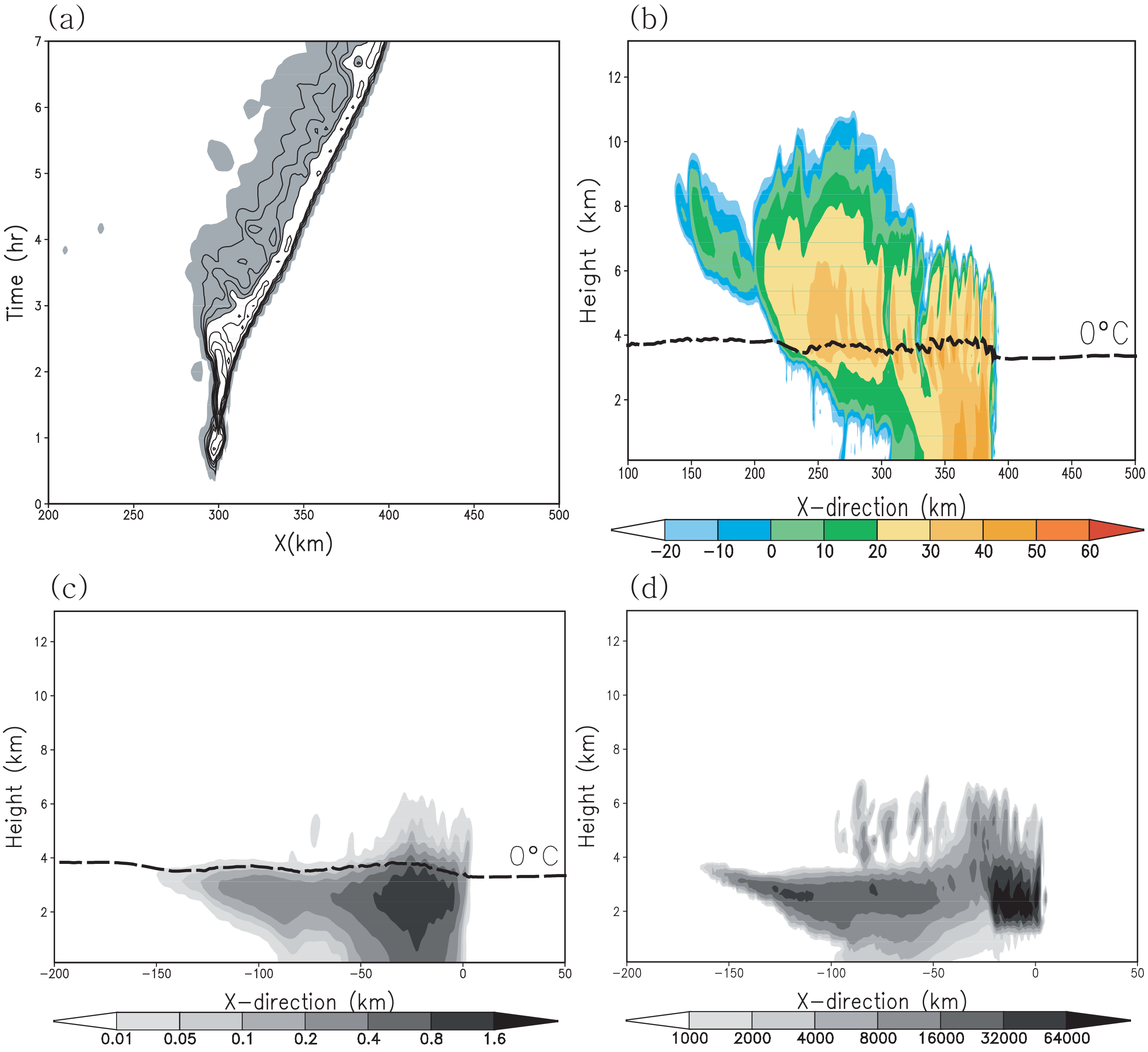

FIG. 11. (a) Hovmöller plots of the surface rainfall rate [mm (10 min)$^{-1}$] and (b) simulated reflectivity (dB*Z*) at 6 h from the WARM experiment, (c) the rain mixing ratio (g kg^{-1}), and (d) for the rain number concentration (m^{-3}) averaged between 5 and 6 h obtained from the WARM experiment.

convective core region and widespread stratiform precipitation (cf., Figs. 5a and 11a). Note that narrower distribution of precipitation in the convective core from the WARM run resembles the feature simulated by the WSM run (see Fig. 5b). Enhanced stratiform precipitation activity is visible in the radar reflectivity. The mixing ratios of rainwater (Fig. 11c) also show an intermediate characteristic (see Figs. 9a,b), but the corresponding rain number concentrations (Fig. 11d) are very similar to the WDM run in terms of magnitude (see Figs. 9c,d).

Because all the warm-rain physics for clouds and rain are identical for both the WARM and WSM experiments, the differences between the two may be caused by the effects of the rain number concentrations. The order of N_R is 10^3 and 10^4 m^{-3} in the WSM and WARM experiments, respectively, whereas the magnitude of N_R is similar for both the WARM and WDM experiments. Thus, more raindrops with relatively small size in the double-moment approach were produced by the added melting processes of snow and graupel, leading to larger mixing ratios for rain and enhanced reflectivity near the freezing level. The higher N_R in the double-moment approach leads to enhanced evaporation below, with a few raindrops falling to the ground over the stratiform region. Differences in perturbation potential

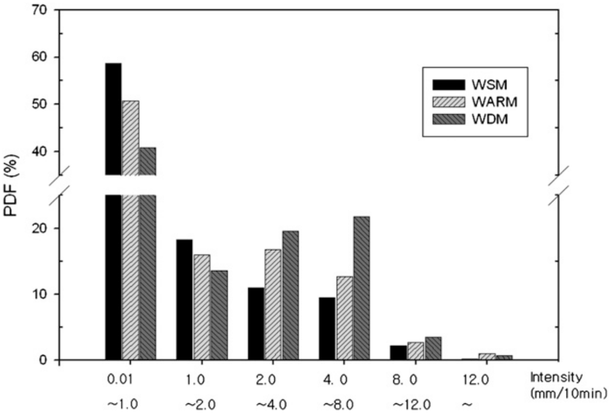

FIG. 12. PDF of 10-min accumulated rainfall intensity from three different experiments.

temperature between the WARM and WSM simulations confirmed the effective evaporation process of small drops (data not shown).

Meanwhile, it is confirmed that an intercept parameter of rain N_{0R} in the convective core is smaller than that in the stratiform cloud region in the case of the WARM experiment. The WARM experiment can reproduce the observed shift of N_{0R} with a more flexible raindrop size distribution (Joss et al. 1970; Waldvogel 1974). Similar distributions of N_R between the WARM and WDM experiments confirm that the double-moment approach in the WDM6 microphysics scheme improves the raindrop property, reducing the light precipitation. The WSM cannot explain the shift of N_{0R} from the weak convection region to the strong convection region by adopting a constant value for N_{0R}, which corresponds to the value describing the medium and strong convection activity region in the Waldvogel (1974), even though direct comparison is not possible between the values from the idealized squall-line simulation and the ones from the observation. Waldvogel (1974) mentioned that the N_{0R} decreases with increasing convective activity and the shift of N_{0R} could occur in the stratiform region with the changes in microphysics of hydrometeors. Waldvogel (1974) also showed that in the continuous widespread rain case there was a change in the magnitude of N_{0R}, which can vary between the 10^6 m^{-4} and 10^8 m^{-4}.

Figure 12 shows the probability distribution functions (PDFs) of the WRF-simulated surface rainfall intensity. Compared to the results from the WSM experiment, the WDM experiment tends to reduce the light precipitation activity, whereas the increase of moderate and heavy precipitation is evident. The WARM experiment increases (decreases) the light (heavy) precipitation toward the results from the WSM experiment but is not entirely compensated. The comparisons of PDFs from the three experiments, together with the figures shown in this section, ascertain that the reduction of light and moderate precipitation activities in the WDM6 physics against the WSM6 physics is a combined effect of prognostic rain number concentration and warm-rain microphysics introduced in the WDM6, whereas the increase of heavy precipitation is largely due to the warm-rain microphysics shown in Table 1.

b. *CCN effects on precipitation*

The impact of the aerosol concentrations on hydrometeors and surface precipitation can be evaluated by varying the number and mass of aerosols at the initial time, as is reflected in the changes in the number concentrations of CCN. The control experiment, which employs the initial CCN number concentration as 100 cm^{-3} in the WDM6 microphysics scheme, was evaluated on an idealized 2D thunderstorm test bed in section 3a. Additional experiments with six different initial CCN number concentrations from 500 cm^{-3} to 8000 cm^{-3} were conducted. Here, we will focus on the properties of cloud and rain substances and surface precipitation in response to the aerosol concentrations to figure out the intrinsic behaviors of the WDM6 scheme, which could provide guidance to the study of aerosol–cloud feedback. The evolutionary feature of the simulated surface precipitation becomes complicated with respect to the varying CCN number concentration after the first cell at 4 h; thus, only the results averaged for the first 4 h of integration time are shown.

Figure 13 shows the simulated cloud and properties with different initial CCN number concentrations. Here, N_C monotonically increases as the initial CCN number concentration increases (Fig. 13a). The N_C varies from 25.51 to 2035.61 cm^{-3} in response to the CCN number concentrations increasing from 100 to 8000 cm^{-3} over the cloudy area. The increase of N_C with the CCN number indicates enhanced activation of aerosols to form cloud droplets, as have been found in previous numerical modeling studies (i.e., Fan et al. 2007; Li et al. 2008). In contrast, the effective droplet size decreases with an increasing CCN number concentration, reflecting a reduced supersaturation when a large number of cloud droplets compete for a fixed amount of available water vapor (Fig. 13b). Raindrop properties show opposite responses with respect to the varying CCN number concentration compared with cloud droplet properties (Figs. 13c,d). In general, the simulated number concentration of raindrops decreases rapidly with an increasing CCN number concentration because a large number of small cloud droplets hinder the effective autoconversion process from cloud water to rain. However, the slightly increasing trend of the simulated rain number concentration

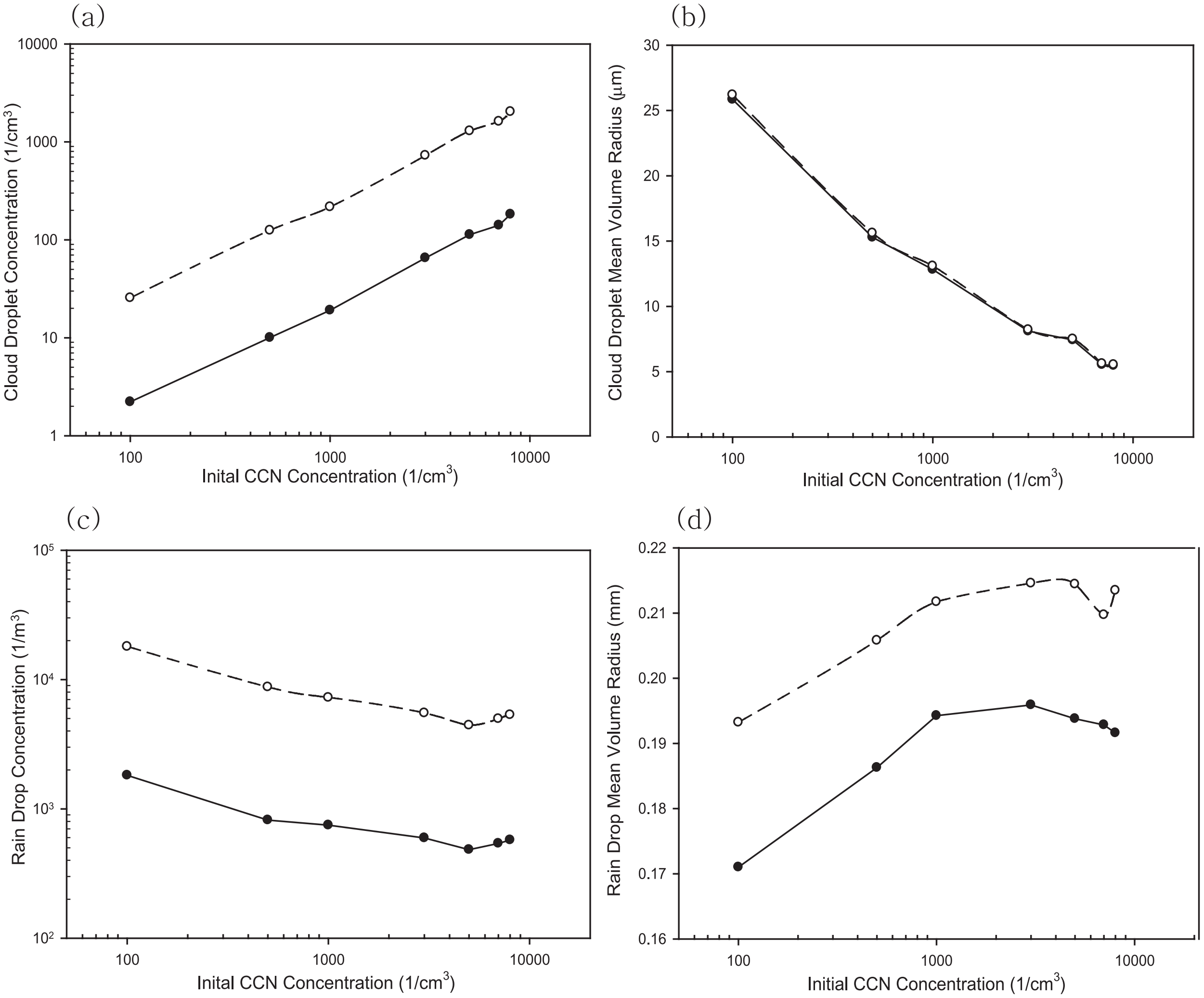

FIG. 13. (a) Modeled number concentration and (b) effective mean volume radius of cloud droplets, which are obtained from whole domain-averaged values (solid) and cloud area-averaged ones (dashed) during the first 4-h integration time period, respectively, under varying initial CCN number concentrations with the WDM6 schemes. (c),(d) The corresponding results for the raindrops . Cloudy area is defined as either $q_C + q_I > 0.01$ g kg^{-1} or $q_R + q_S > 0.01$ g kg^{-1}.

is shown for CCN greater than 5000 cm^{-3}, which is due to the saturated environment with an enhanced evaporation rate of a large number of small cloud droplets, as the CCN number concentration increases. The raindrops are not converted into the cloud droplets under the saturated environment. Comparatively, raindrop-mean-volume radius shows the opposite response with variations in the CCN number concentration.

Domain-averaged total precipitation with respect to the initial CCN number concentration is shown in Fig. 14. When the CCN number concentration is relatively small, the total precipitation increases with the CCN number concentration from 100 cm^{-3} to 3000 cm^{-3}. The precipitation amount decreases sharply when the CCN number concentration is over 3000 cm^{-3}. The enhanced precipitation with increasing aerosols at lower CCN is explained by the suppressed conversion of cloud droplets to raindrops but enhanced convective strength, which causes less efficient warm rain but more mixed-phase processes, corresponding with the results of Li et al. (2008). Meanwhile, the decreased precipitation in the high-CCN condition is due to the extremely suppressed conversion from cloud droplets to raindrops. Li et al. (2008) simulated deep cumulus under a relatively small wind shear and humid environment and found out that the hydrometeors cannot grow to a sufficiently large size to survive evaporation with extremely high aerosol condition. Thus, the total precipitation is decreased or completely suppressed. However, the responses of aerosols on precipitation could be nonmonotonic and vary

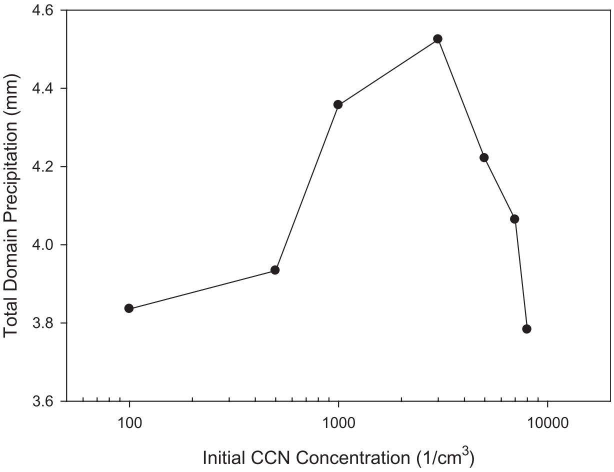

FIG. 14. Total surface precipitation with respect to the initial CCN number concentration with the WDM6 microphysics scheme.

under different meteorological and aerosol conditions because of the complicated coupling between the cloud microphysics and dynamics (Seifert and Beheng 2006; Li et al. 2008).

5. Concluding remarks

A new bulk microphysics scheme, the WDM6, has been developed by adding a double-moment treatment for the warm-rain process into the WSM6 scheme. The CCN number concentration is also predicted in the WDM6 scheme, based on the relationships between the number of activated CCN and environmental supersaturation value. The new scheme is implemented into the WRF model and tested within a 2D idealized thunderstorm test bed. The WDM6 microphysics scheme specifies the particle size distributions of various hydrometeors types and typically solves prognostic equations of a mixing ratio and number concentration for each type as in other double-moment microphysics schemes of regional-scale models. The major differences between the WDM6 and other double-moment bulk microphysics schemes in the WRF model (e.g., Thompson et al. 2008; Morrison et al. 2005) is the inclusion of prognostic equations for the cloud water and CCN number concentrations, which allows for the possibility of investigating the aerosol effects on cloud properties and the precipitation process. The number concentrations of ice species such as graupel, snow, and ice are diagnosed following the ice-phase microphysics of Hong et al. (2004), whereas the number concentrations of ice phases are predicted in the Thompson and Morrison scheme (i.e., number concentration of cloud ice in the Thompson scheme, and cloud ice, graupel, and snow in the Morrison scheme).

The overall resemblance of the storm morphology and its evolutionary features from the idealized 2D experiments with the WSM6 and WDM6 schemes ensures that the predicted number concentrations for cloud and rainwater, coupled with the CCN processes, are correctly implemented. In addition, varying the CCN number concentration has nonmonotonic impacts on rainfall amount. To be consistent with the previous observational studies (Waldvogel 1974; Tokay and Short 1996), relatively high drop concentrations in the convective core due to collision–coalescence versus low drop concentrations in the stratiform region due to the enhanced rain formation by the melting process of ice particles are reproduced by the double-moment approach. Conversely, in the single-moment scheme the boundary between the convective and stratiform regions is unclear and the distribution of the rain number concentration is uniform in the vertical direction, with relatively small rain number concentrations and weak radar reflectivity compared to the double-moment scheme. The overall increase of raindrop concentrations in the double-moment scheme results in excessive evaporation in the stratiform region, which leads to a significant reduction of surface rainfall.

Additionally, the impact of the double-moment scheme over the single-moment scheme on the simulated storm differs in Morrison et al. (2009) and in this study. Morrison et al. (2009) showed that the reduced rain evaporation rates with larger mean drop size over the trailing stratiform region in the double-moment method compared to the single-moment method leads to enhanced precipitation, whereas increased rain evaporation rates in a convective region show the opposite response. This study shows a different response over the stratiform/convective core region. The determination of what causes different responses from the single- to double-moment approaches between Morrison et al. (2009) and the results from this study is not straightforward because fundamental differences exist between the double-moment schemes in both studies. The absence of enhanced melting processes of snow and graupel in Morrison et al. (2009) can partly explain the different responses. Meanwhile, Li et al. (2009a) showed that the bin microphysics scheme tends to produce enhanced light rain with a suppressed evaporation rate as compared to the bulk microphysics scheme. Morrison et al. (2009), Li et al. (2009a,b), and the present study indicate that the rain number concentration plays an important role in determining the precipitation rate and storm morphology because it modulates the related microphysics terms, in particular, the evaporation rate.

As demonstrated in the idealized 2D frameworks in this study, behaviors of the WDM6 scheme against the

WSM6 scheme, such as enhanced radar reflectivity and the weakened (strengthened) light (heavy) precipitation activities, would alleviate several systematic biases of the WSM6 scheme with little reflectivity (J. Kain 2008, personal communication) and excessive light precipitation (Shi et al. 2007). However, a more robust evaluation of the hydrometeor profile including the CCN distribution is necessary. A preliminary evaluation of the WDM6 scheme against the WSM6 scheme confirmed that the precipitation forecasts over Korea from June to August 2008 are generally improved in terms of the skill statistics (Hong and Lim 2009).

One of the strengths of the WDM6 scheme is its ability to represent major characteristics of the double-moment microphysics scheme in terms of radar reflectivity and number concentrations of rain, as seen in observational studies at a modest computational cost (the WDM6 code has a 30% extra computing burden in terms of the total run time than the WSM6 code in a 3D real-case run), in order for the scheme to be applicable not only in a nonhydrostatic mesoscale model for weather forecasts but also in global models for climate studies. Not reported in this study, another double-moment scheme, the WRF double-moment 5-class (WDM5) scheme, was also developed by adding the number concentrations for warm-phase physics to the WRF single-moment 5-class (WSM5) scheme. This simplicity is theoretically based on the fact that the prediction of ice-phase number concentrations has significantly less impact on the results than the prediction of warm-phase concentrations in deep convective cases (Morrison et al. 2009).

The advantage in computation also makes the scheme suitable for realistic 3D numerical experiments such as the large-eddy simulation (LES) of precipitating stratus to detailed studies of warm precipitating systems. Part of the success of this double-moment scheme relies on its capacity to handle explicit representation of the CCN number concentration, even though the quantitative evaluation of the simulated CCN should be evaluated. Incorporation of a subgrid vertical velocity derived from the planetary boundary layer and turbulence diffusion scheme into the CCN activation process (Ghan et al. 1997; Morrison et al. 2005; Morrison and Pinto 2005) would be more physically reasonable in estimating $S_{\max}$, which can be pursued in future studies. The new double-moment schemes introduced in the present study, the WDM6 and the WDM5 schemes, were implemented in WRF version 3.1, which was released in April 2009.

Acknowledgments. This work was supported by the Basic Science Research Program through the National Research Foundation of Korea (NRF) funded by the Ministry of Education, Science and Technology (2009-0080658). The authors would like to express their gratitude to Jimy Dudhia for sharing ideas in the early stage of WDM6 development. Appreciation is also extended to Hugh Morrison and Jean-Pierre Pinty for helpful discussions regarding the double-moment issues.

APPENDIX

Microphysical Processes for the Prediction of Number Concentration in the WDM6 Scheme

a. *Production term for CCN number concentration*

$$S_{\mathrm{CCN}} = -\mathrm{Ncact} + \mathrm{Ncevp} \tag{A1}$$

1) ACTIVATION (NCACT)

The activation rate of the CCN number concentration can be expressed as

$$\mathrm{Ncact}(\mathrm{m}^{-3}\,\mathrm{s}^{-1}) = \frac{\max\left\{0, (n + N_C)\min[1, (S_W/S_{\max})^k] - N_C\right\}}{\Delta t}, \tag{A2}$$

where nucleation growth occurs with the supersaturation environment.

The CCN number concentration shows a small variation in the vertical direction. Yum and Hudson (2002) reported the CCN value of 163 cm^{-3} for the maritime and 1023 cm^{-3} for the continental-type air mass with the 0.6% supersaturation in the Atlantic Stratocumulus Transition Experiment (ASTEX) measurement project. The authors of the present study understand that accurate 3D CCN information is an important aspect in model simulation. However, obtaining CCN information in both the horizontal and vertical directions in real time is difficult. In this study, the typical value of marine-type CCN (100 cm^{-3}) was chosen, which is considered to be the initial value of CCN number concentration. In the preliminary tests, the initial CCN number concentration was determined to not have much impact on the cloud and precipitation process for the double or half value of the CCN number concentration in the WDM6 scheme.

2) EVAPORATION (NCEVP)

The drop concentration does not change during the condensation. The drop concentration can be changed, however, when cloud drops are completely evaporated. Based on CP2000, evaporated cloud droplets are added into the total CCN population:

$$\mathrm{Ncevp}(\mathrm{m}^{-3}\,\mathrm{s}^{-1}) = \frac{N_C}{q_C}(\mathrm{Pcond}). \qquad \text{(A3)}$$

Any other source and sink terms including the scavenging process by precipitation are neglected.

b. *Production term for cloud droplet number concentration*

The production term for cloud water may be written for two temperature regimes:

- If the temperature is below 0°C ($T < T_0$)

$$\begin{aligned} S_C = {} & \mathrm{Ncact} - \mathrm{Nraut} - \mathrm{Nccol} - \mathrm{Nracw} - \mathrm{Nsacw} \\ & - \mathrm{Ngacw} + \mathrm{Nrevp} - \mathrm{Ncevp} - \mathrm{Nihmf} - \mathrm{Nihtf} \end{aligned} \qquad \text{(A4)}$$

- If the temperature is above 0°C ($T \geq T_0$), then

$$\begin{aligned} S_C = {} & \mathrm{Ncact} - \mathrm{Nraut} - \mathrm{Nccol} - \mathrm{Nracw} - \mathrm{Nsacw} \\ & - \mathrm{Ngacw} + \mathrm{Nrevp} - \mathrm{Ncevp} - \mathrm{Nihmf} + \mathrm{Nihtf} \end{aligned} \qquad \text{(A5)}$$

1) ACTIVATION (NCACT)

Ncact is presented by (A2).

2) AUTOCONVERSION (NCACT)

The autoconversion parameterization is obtained from the parameterization proposed by CP2000 and can be expressed as

$$\mathrm{Nraut}(\mathrm{m}^{-3}\,\mathrm{s}^{-1}) = 3.5 \times 10^9 \frac{\rho_a L}{\tau}, \qquad \text{(A6.1)}$$

where L denotes the characteristic water content, and τ represents time-scale characteristics and are represented in Eqs. (9.1) and (9.2) in the text, respectively.

When the rain mixing ratio reaches 1.2 × L, the autoconversion process will switch into the feeding regime. In the feeding regime, Nraut is expressed as the following:

$$\mathrm{Nraut}(\mathrm{m}^{-3}\,\mathrm{s}^{-1}) = \frac{N_R}{q_R}(\mathrm{Praut}). \qquad \text{(A6.2)}$$

The autoconversion process occurs only if $D_C > 15\ \mu\mathrm{m}$, where D_C represents the mean-volume-drop diameter of rainwater and is expressed as

$$D_C = \left[\frac{M_C(3)}{M_C(0)}\right]^{1/3} = \frac{1}{\lambda_C}\left[\frac{\Gamma(\nu_C + 3/\alpha_C)}{\Gamma(\nu_C)}\right]^{1/3} = \frac{1}{\lambda_C}. \qquad \text{(A7)}$$

3) SELF-COLLECTIONS (NCCOL)

The self-collection of CP2000, which is obtained from the analytical integration of the stochastic collection equation, was adopted by the authors. This process represents the coalescence of particles in a manner that the resulting particle remains within the same hydrometeor's category; thus, leading to changes only in number concentration but not in the mixing ratio:

- If $D_C \geq 100\ \mu\mathrm{m}$, then

$$\mathrm{Nccol}(\mathrm{m}^{-3}\,\mathrm{s}^{-1}) = K_1 N_C^2 \frac{\Gamma(\nu_C + 3/\alpha_C)}{\Gamma(\nu_C)\lambda_C^3} = \frac{K_1 N_C^2}{\lambda_C^3}. \qquad \text{(A8.1)}$$

- If $D_C < 100\ \mu\mathrm{m}$, then

$$\mathrm{Nccol}(\mathrm{m}^{-3}\,\mathrm{s}^{-1}) = K_1 N_C^2 \frac{\Gamma(\nu_C + 3/\alpha_C)}{\Gamma(\nu_C)\lambda_C^3} = \frac{K_1 N_C^2}{\lambda_C^3}. \qquad \text{(A8.2)}$$

4) ACCRETION (NRACW, NSACW, AND NGACW)

Number concentration of cloud water decreases by the accretion of other species, such as rainwater, snow, and ice.

Accretion of cloud water by rain follows the accretion of CP2000, which is turned off until the rain mixing ratio reaches 1.2 × L. Nracw is divided into two regimes according to the magnitude of D_R

- If $D_C \geq 100\ \mu\mathrm{m}$, then

$$\begin{aligned} & \mathrm{Nracw}(\mathrm{m}^{-3}\,\mathrm{s}^{-1}) \\ & = K_1 N_C N_R \left[\frac{\Gamma(\nu_C + 3/\alpha_C)}{\Gamma(\nu_C)\lambda_C^3} + \frac{\Gamma(\nu_R + 3/\alpha_R)}{\Gamma(\nu_R)\lambda_R^3}\right] \\ & = K_1 N_C N_R \left(\frac{1}{\lambda_C^3} + \frac{24}{\lambda_R^3}\right). \end{aligned} \qquad \text{(A9.1)}$$

- If $D_R \geq 100\ \mu\text{m}$, then

$$
\begin{aligned}
&\text{Nracw}(\text{m}^{-3}\,\text{s}^{-1})\\
&\quad = K_2 N_C N_R \left[\frac{\Gamma(\nu_C + 6/\alpha_C)}{\Gamma(\nu_C)\lambda_C^6} + \frac{\Gamma(\nu_R + 6/\alpha_R)}{\Gamma(\nu_R)\lambda_R^6}\right]\\
&\quad = K_2 N_C N_R \left(\frac{2}{\lambda_C^6} + \frac{5040}{\lambda_R^6}\right),
\end{aligned}
\tag{A9.2}
$$

where D_R represents the mean-volume-drop diameter of rainwater and is expressed as

$$
D_R = \left[\frac{M_R(3)}{M_R(0)}\right]^{1/3} = \frac{1}{\lambda_R}\left[\frac{\Gamma(\nu_R + 3/\alpha_R)}{\Gamma(\nu_R)}\right]^{1/3} = \frac{1}{\lambda_R}(24)^{1/3}.
\tag{A10}
$$

The collection of cloud water by snow is assumed to follow the continuous collection equation suggested by Ikawa and Saito (1991) and can be expressed as

$$
\begin{aligned}
&\int \frac{d\text{Prob}(D_S)}{dt}\, dN_{D_S}\\
&\quad = \iint \frac{\pi}{4} D_S^2 V_S(D_S) E_{\text{SC}} N_{0S} \exp[-(\lambda_S D_S)] 3 N_C \lambda_C^3 D_C^2 \exp[-(\lambda_C D_C)^3]\, dD_S\, dD_C\\
&\quad = \frac{\pi}{4} a_S E_{\text{SC}} N_{0\text{S}} N_C \left(\frac{\rho_0}{\rho_a}\right)^{1/2} \left[\frac{\Gamma(3 + b_S)}{\lambda_S^{3+b_S}}\right],
\end{aligned}
\tag{A11}
$$

with the assumption that cloud water does not sediment, and its size is small enough to ignore the comparison of the snow size. Thus, the accretion of cloud water by snow can be expressed in a bulk formula as follows:

$$
\text{Nsacw}(\text{m}^{-3}\,\text{s}^{-1}) = \frac{\pi a_S E_{\text{SC}} N_{0\text{S}} N_C}{4} \left(\frac{\rho_0}{\rho_a}\right)^{1/2} \left[\frac{\Gamma(3 + b_S)}{\lambda_S^{3+b_S}}\right].
\tag{A12}
$$

The accretion of cloud water by graupel is similar to (A11) and is expressed as

$$
\text{Ngacw}(\text{m}^{-3}\,\text{s}^{-1}) = \frac{\pi a_G E_{\text{GC}} N_{0\text{G}} N_C}{4} \left(\frac{\rho_0}{\rho_a}\right)^{1/2} \left[\frac{\Gamma(3 + b_G)}{\lambda_G^{3+b_G}}\right].
\tag{A13}
$$

The mass-weighted terminal velocity for the snow and graupel species suggested by Dudhia et al. (2008) is used in the present study.

5) EVAPORATION (NREVP AND NCEVP)

If the mean-volume-drop diameter of rainwater becomes smaller than 82 μm and the air is subsaturated with respect to water, then all raindrops are converted into cloud drops,

$$
\text{Nrevp}(\text{m}^{-3}\,\text{s}^{-1}) = \frac{N_R}{\Delta t}.
\tag{A14}
$$

Based on Khairoutdinov and Kogan (2000), changes in mass (Prevp_rc) corresponding to the raindrop evaporation are added to the cloud water mass:

$$
\text{Prevp\_rc}(\text{kg}\,\text{kg}^{-1}\,\text{s}^{-1}) = \frac{q_R}{N_R}(\text{Nrevp}).
\tag{A15}
$$

Ncevp is also presented by (A3).

6) FREEZING (NIHTF AND NIHMF)

According to Wisner et al. (1972) and Bigg (1953), the decreased number concentration rate of cloud water by the heterogeneous freezing of cloud water is given by

$$
\begin{aligned}
\text{Nihtf}(\text{m}^{-3}\,\text{s}^{-1}) &= \int \frac{\pi B' D_C^3}{6} \{\exp[A'(T_0 - T)] - 1\} 3 N_C \lambda_C^3 D_C^2 \exp[-(\lambda_C D_C)^3]\, dD_C\\
&= \frac{\pi B' N_C \lambda_C^3}{6} \{\exp[A'(T_0 - T)] - 1\} \int D_C^3 3 D_C^2 \exp[-(\lambda_C D_C)^3]\, dD_R\\
&= \frac{\pi B' N_C}{6} \{\exp[A'(T_0 - T)] - 1\} \lambda_C^{-3}.
\end{aligned}
\tag{A16}
$$

This term represents another sink term of the cloud droplets number concentration and the process occurs when $-40°C < T < T_0$. The homogeneous freezing of cloud water (Nihmf) also serves as a sink term for cloud droplets when the temperature is below −40°C:

$$\mathrm{Nihmf}(\mathrm{m}^{-3}\,\mathrm{s}^{-1}) = \frac{N_C}{\Delta t}. \qquad \text{(A17)}$$

7) MELTING (NIMLT)

Melting of cloud ice to form cloud water is assumed to occur instantaneously, if $T \geq T_0$ and is given by

$$\mathrm{Nimlt}(\mathrm{m}^{-3}\,\mathrm{s}^{-1}) = \frac{N_1}{q_1}(\mathrm{Pimlt}). \qquad \text{(A18)}$$

c. Production term for raindrop number concentration

The production term for rain may be written for two temperature regimes:

- If the temperature is below 0°C ($T < T_0$), then

$$S_R = \mathrm{Nraut} - \mathrm{Nrcol} - \mathrm{Nsacr} - \mathrm{Ngacr} - \mathrm{Niacr} - \mathrm{Nrevp} - \mathrm{Ngfrz}. \qquad \text{(A19)}$$

- If the temperature is above 0°C ($T \geq T_0$), then

$$S_R = \mathrm{Nraut} - \mathrm{Nrcol} - \mathrm{Nrevp} + \mathrm{Nsmlt} + \mathrm{Ngmlt} + \mathrm{Nseml} + \mathrm{Ngeml}. \qquad \text{(A20)}$$

1) AUTOCONVERSION (NRAUT)

Nraut is presented by (A6).

2) SELF-COLLECTION AND RAINDROP BREAKUP (NRCOL)

Collisional breakup is the only break up effect that is considered in the following formula for its significant contribution to the slope parameter λ at the edge of raindrop distributions (Srivastava 1978). The break up process can be interpreted as a perturbation affecting the formulation of the raindrop self-collection term, as suggested in CP2000. The self-collection can be written as the following:

- If $D_C \geq 100\ \mu\mathrm{m}$, then

$$\mathrm{Nrcol}(\mathrm{m}^{-3}\,\mathrm{s}^{-1}) = K_2 N_R^2 \frac{\Gamma(\nu_R + 6/\alpha_R)}{\Gamma(\nu_R)\lambda_R^6} = K_2 N_R^2 \frac{\Gamma(8)}{\Gamma(1)\lambda_R^6} = 5040 \frac{K_2 N_R^2}{\lambda_C^6}; \qquad \text{(A21.1)}$$

- if $100\ \mu\mathrm{m} \leq D_R < 600\ \mu\mathrm{m}$, then

$$\mathrm{Nrcol}(\mathrm{m}^{-3}\,\mathrm{s}^{-1}) = K_1 N_R^2 \frac{\Gamma(\nu_R + 3/\alpha_R)}{\Gamma(\nu_R)\lambda_R^3} = K_1 N_R^2 \frac{\Gamma(5)}{\Gamma(2)\lambda_R^3} = 24 \frac{K_1 N_R^2}{\lambda_C^3}; \quad \text{and} \qquad \text{(A21.2)}$$

- if $600\ \mu\mathrm{m} \leq D_R < 2000\ \mu\mathrm{m}$, then

$$\mathrm{Nrcol}(\mathrm{m}^{-3}\,\mathrm{s}^{-1}) = E_C K_1 N_R^2 \frac{\Gamma(\nu_R + 3/\alpha_R)}{\Gamma(\nu_R)\lambda_R^3} = E_C K_1 N_R^2 \frac{\Gamma(5)}{\Gamma(2)\lambda_R^3} = 24 E_C \frac{K_1 N_R^2}{\lambda_R^3}, \qquad \text{(A21.3)}$$

where $E_C = \exp[-2.5 \times 10^3(D_R - 6 \times 10^{-4})]$

The self-collection process of rain is turned off until the rain mixing ratio reaches $1.2 \times L$.

3) ACCRETION (NSACR, NGACR, AND NIACR)

The accretion of rain by snow is also assumed to follow the continuous collection equation, which can be expressed as

$$\int \frac{d\mathrm{Prob}(D_S)}{dt}\, dN_{D_S} = \iint \pi \left(\frac{D_S + D_R}{2}\right)^2 \times |V_S(D_S) - V_R(D_R)| \times E_{\mathrm{SR}} N_{0\mathrm{S}} \times \exp[-(\lambda_S D_S)] N_R \lambda_R^2 D_R \exp[-(\lambda_R D_R)]\, dD_S\, dD_R. \qquad \text{(A22)}$$

Assuming the difference in the sedimentation velocity for snow and rain with respect to the diameter of snow can be neglected, the loss term for accretion of rain by snow is given by

$$\mathrm{Nsacr}(\mathrm{m}^{-3}\,\mathrm{s}^{-1}) = \pi E_{\mathrm{SR}} N_{0\mathrm{S}} N_R |V_S - V_R| \times \left(\frac{0.5}{\lambda_S^3} + \frac{1}{\lambda_S^2 \lambda_R^1} + \frac{1.5}{\lambda_S^1 \lambda_R^2}\right). \qquad \text{(A23)}$$

Similarly, the accretion of rain by graupel is as follows:

$$\mathrm{Ngacr}(\mathrm{m}^{-3}\,\mathrm{s}^{-1}) = \pi E_{\mathrm{GR}} N_{0\mathrm{G}} N_R |V_G - V_R| \times \left(\frac{0.5}{\lambda_G^3} + \frac{1}{\lambda_G^2 \lambda_R^1} + \frac{1.5}{\lambda_G^1 \lambda_R^2}\right). \qquad \text{(A24)}$$

The loss term of the rain number concentration by the accretion of rain by cloud ice is obtained by multiplying the rate at which a cloud ice particle collides with a raindrop (assuming the probability for the existence of a rain particle is uniform throughout the volume) by the number concentration of cloud ice. The collection of rain by cloud ice is also assumed to follow the continuous equation and is given by

TABLE A1. List of symbols.

Symbol	Description	Value	SI units
A'	Constant in raindrop freezing equation	0.66	K^{-1}
a_G	Empirical formula of V_G	330	$\mathrm{m}^{1-b}\ \mathrm{s}^{-1}$
a_R	Empirical formula of V_R	841.9	$\mathrm{m}^{1-b}\ \mathrm{s}^{-1}$
a_S	Empirical formula of V_S	11.72	$\mathrm{m}^{1-b}\ \mathrm{s}^{-1}$
B'	Constant in raindrop freezing equation	100	$\mathrm{m}^{-3}\ \mathrm{s}^{-1}$
b_G	Empirical formula of V_G	0.8	
b_R	Empirical formula of V_R	0.8	
b_S	Empirical formula of V_S	0.41	
D_C	Cloud water diameter		m
D_R	Rain diameter		m
D_S	Snow diameter		m
D_X	Hydrometeor X diameter		m
E_C	Rain collection efficiency		
E_{GC}	Graupel–cloud water collection efficiency	1	
E_{GR}	Graupel–rain collection efficiency	1	
E_{RC}	Rain–cloud water collection efficiency	1	
E_{RI}	Rain–cloud ice collection efficiency	1	
E_{SC}	Snow–cloud water collection efficiency	1	
E_{SR}	Snow–rain collection efficiency	1	
K_1	Long's collection kernel coefficient	3.03×10^3	$\mathrm{m}^{-3}\ \mathrm{s}^{-1}$
K_2	Long's collection kernel coefficient	2.59×10^{15}	$\mathrm{m}^{-3}\ \mathrm{s}^{-1}$
k	Parameter for the CCN activation	0.6	
L	Characteristic water content		
M_C	Average mass of a cloud water		kg
$M_C(p)$	P-moment of the cloud water size distribution		
$M_R(p)$	P-moment of the raindrop size distribution		
N_C	Number concentration of cloud water		m^{-3}
N_{DR}	Integrated raindrop size distribution along the entire range of the diameter		m^{-2}
N_{DS}	Integrated snow size distribution along the entire range of the diameter		m^{-2}
N_X	Number concentration of hydrometeor X		m^{-3}
$n_X(D_X)$	Number concentration of hydrometeor X of diameter D_X		m^{-4}
$N_{0\mathrm{G}}$	Intercept parameter of graupel	4×10^6	m^{-4}
$N_{0\mathrm{R}}$	Intercept parameter of rain	8×10^6	m^{-4}
$N_{0\mathrm{S}}$	Intercept parameter of snow	$2 \times 10^6 \exp[0.12(T - T_0)]$	m^{-4}
n	Initial value of the cloud condensation nuclei	10^8	m^{-3}
n_a	Activated CCN number concentration		m^{-3}
Ncact	Generation rate by activation of the CCN		$\mathrm{m}^{-3}\ \mathrm{s}^{-1}$
Nccol	Generation rate by self-collection of cloud water		$\mathrm{m}^{-3}\ \mathrm{s}^{-1}$
Ncevp	Generation rate by cloud water evaporation		$\mathrm{m}^{-3}\ \mathrm{s}^{-1}$
Ngacr	Generation rate by accretion of rainwater by graupel		$\mathrm{m}^{-3}\ \mathrm{s}^{-1}$
Ngacw	Generation rate by accretion of cloud water by graupel		$\mathrm{m}^{-3}\ \mathrm{s}^{-1}$
Ngeml	Generation rate by enhanced melting of graupel		$\mathrm{m}^{-3}\ \mathrm{s}^{-1}$
Ngfrz	Generation rate by freezing of rainwater to graupel		$\mathrm{m}^{-3}\ \mathrm{s}^{-1}$
Ngmlt	Generation rate by melting of graupel		$\mathrm{m}^{-3}\ \mathrm{s}^{-1}$
Niacr	Generation rate by accretion of rainwater by ice		$\mathrm{m}^{-3}\ \mathrm{s}^{-1}$
Nihmf	Generation rate by homogeneous freezing		$\mathrm{m}^{-3}\ \mathrm{s}^{-1}$
Nihtf	Generation rate by heterogeneous freezing		$\mathrm{m}^{-3}\ \mathrm{s}^{-1}$
Nimlt	Generation rate by melting of ice		$\mathrm{m}^{-3}\ \mathrm{s}^{-1}$
Nracw	Generation rate by accretion of cloud water by rain		$\mathrm{m}^{-3}\ \mathrm{s}^{-1}$
Nraut	Generation rate by autoconversion		$\mathrm{m}^{-3}\ \mathrm{s}^{-1}$
Nrcol	Generation rate by self-collection of rainwater		$\mathrm{m}^{-3}\ \mathrm{s}^{-1}$
Nrevp	Generation rate by evaporation of rainwater		$\mathrm{m}^{-3}\ \mathrm{s}^{-1}$
Nsacr	Generation rate by accretion of rainwater by snow		$\mathrm{m}^{-3}\ \mathrm{s}^{-1}$
Nsacw	Generation rate by accretion of cloud water by snow		$\mathrm{m}^{-3}\ \mathrm{s}^{-1}$
Nseml	Generation rate by enhanced melting of snow		$\mathrm{m}^{-3}\ \mathrm{s}^{-1}$
Nsmlt	Generation rate by melting of snow		$\mathrm{m}^{-3}\ \mathrm{s}^{-1}$
Pcact	Production rate for activation of CCN		$\mathrm{kg}\ \mathrm{kg}^{-1}\ \mathrm{s}^{-1}$

TABLE A1. (*Continued*)

Symbol	Description	Value	SI units
Pcond	Production rate for condensation/evaporation of cloud water		kg kg^{-1} s^{-1}
Pgaci	Production rate for accretion of cloud ice by graupel		kg kg^{-1} s^{-1}
Pgacr	Production rate for accretion of rain by graupel		kg kg^{-1} s^{-1}
Pgacs	Production rate for accretion of snow by graupel		kg kg^{-1} s^{-1}
Pgacw	Production rate for accretion of cloud water by graupel		kg kg^{-1} s^{-1}
Pgaut	Production rate for autoconversion of snow to form graupel		kg kg^{-1} s^{-1}
Pgdep	Production rate for deposition/sublimation rate of graupel		kg kg^{-1} s^{-1}
Pgeml	Production rate induced by enhanced melting rate of graupel		kg kg^{-1} s^{-1}
Pgevp	Production rate for evaporation of melting graupel		kg kg^{-1} s^{-1}
Pgfrz	Production rate for freezing of rainwater to graupel		kg kg^{-1} s^{-1}
Pgmlt	Production rate for melting of graupel to form rain		kg kg^{-1} s^{-1}
Piacr	Production rate for accretion of rain by cloud ice		kg kg^{-1} s^{-1}
Pidep	Production rate for deposition–sublimation rate of ice		kg kg^{-1} s^{-1}
Pigen	Production rate for generation (nucleation) of ice from vapor		kg kg^{-1} s^{-1}
Pihmf	Production rate for homogeneous freezing of cloud water to form cloud ice		kg kg^{-1} s^{-1}
Pihtf	Production rate for heterogeneous freezing of cloud water to form cloud ice		kg kg^{-1} s^{-1}
Pimlt	Production rate for instantaneous melting of cloud ice		kg kg^{-1} s^{-1}
Praci	Production rate for accretion of cloud ice (graupel) by rain		kg kg^{-1} s^{-1}
Pracs	Production rate for accretion of snow by rain		kg kg^{-1} s^{-1}
Pracw	Production rate for accretion of cloud water by rain		kg kg^{-1} s^{-1}
Praut	Production rate for autoconversion of cloud water to form rain		kg kg^{-1} s^{-1}
Prevp	Production rate for evaporation–condensation rate of rain		kg kg^{-1} s^{-1}
Prevp_rc	Production rate for evaporation rate of rain to form cloud water		kg kg^{-1} s^{-1}
Psaci	Production rate for accretion of cloud ice by snow		kg kg^{-1} s^{-1}
Psacr	Production rate for accretion of rain by snow		kg kg^{-1} s^{-1}
Psacw	Production rate for accretion of cloud water by snow		kg kg^{-1} s^{-1}
Psaut	Production rate for autoconversion of cloud ice to form snow		kg kg^{-1} s^{-1}
Psdep	Production rate for deposition–sublimation rate of snow		kg kg^{-1} s^{-1}
Pseml	Production rate induced by enhanced melting of snow		kg kg^{-1} s^{-1}
Psevp	Production rate for evaporation of melting snow		kg kg^{-1} s^{-1}
Psmlt	Production rate for melting of snow to form cloud water		kg kg^{-1} s^{-1}
Prob(D_R)	Probability density function of rain of diameter D_R		
Prob(D_S)	Probability density function of rain of diameter D_S		
q_C	Mixing ratio of cloud water		kg kg^{-1}
q_{C0}	Critical mixing ratio of cloud water		kg kg^{-1}
q_G	Mixing ratio of graupel		kg kg^{-1}
q_I	Mixing ratio of ice crystal		kg kg^{-1}
q_R	Mixing ratio of rain		kg kg^{-1}
q_S	Mixing ratio of snow		kg kg^{-1}
q_X	Mixing ratio of hydrometeor X		kg kg^{-1}
r_{act}	Radius of activated CCN drops	1.5	m
S_C	Sum of production rate for cloud water number concentration		m^{-3} s^{-1}
S_{CCN}	Sum of production rate for CCN number concentration		m^{-3} s^{-1}
S_R	Sum of production rate for rain number concentration		m^{-3} s^{-1}
$S_{\max}$	Super saturation needed to activate the total particle account $n + N_C$	1.0048	
S_W	Saturation ratio with respect to water		
T	Temperature		K
T_0	Reference temperature	273.16	K
V_G	Mass-weighted fall speed of graupel		m s^{-1}
V_R	Mass-weighted fall speed of rain		m s^{-1}
V_S	Mass-weighted fall speed of snow		m s^{-1}
V_X	Mass-weighted fall speed of hydrometeor X		m s^{-1}

TABLE A1. (*Continued*)

Symbol	Description	Value	SI units
$V_{\mathrm{NR}}(D_R)$	Fallspeed of rain number of diameter D_R		m s^{-1}
$V_R(D_R)$	Fallspeed of snowflakes of diameter D_R		m s^{-1}
$V_S(D_S)$	Fallspeed of snowflakes of diameter D_S		m s^{-1}
$\overline{V}_{\mathrm{NR}}$	Number-weighted fallspeed of rain		m s^{-1}
α_C	Dispersion parameter of the generalized gamma distribution law for the cloud water	3	
α_R	Dispersion parameter of the generalized gamma distribution law for the rainwater	1	
α_X	Dispersion parameter of the generalized gamma distribution law for the hydrometeor X		
ρ_a	Air density		kg m^{-3}
ρ_W	Density of water	10^3	kg m^{-3}
ρ_0	Density of air at reference state	1.28	kg m^{-3}
Δt	Time step for cloud microphysics		s
Γ	Complete gamma function		
λ_C	Slope of cloud water size distribution		m^{-1}
λ_G	Slope of graupel size distribution		m^{-1}
λ_R	Slope of rain size distribution		m^{-1}
λ_S	Slope of snow size distribution		m^{-1}
λ_X	Slope of hydrometeor X size distribution		m^{-1}
μ	Dynamic viscosity of air	1.718×10^{-5}	g m^{-1} s^{-1}
ν_C	Dispersion parameter of the generalized gamma distribution law for the rainwater	1	
ν_R	Dispersion parameter of the generalized gamma distribution law for the cloud water	2	
ν_X	Dispersion parameter of the generalized gamma distribution law for the hydrometeor X		
τ	Time-scale of autoconversion process		
σ_C	Standard deviation of cloud droplet distribution		

$$\begin{aligned}\mathrm{Niacr}(\mathrm{m^{-3}\,s^{-1}}) &= \left[\frac{d\mathrm{Prob}(D_R)}{dt}\right] \times N_I\\ &= \left[\frac{\pi}{4}\rho D_R^2 V_R(D_R)\frac{1}{\rho}N_{\mathrm{DR}}E_{\mathrm{RI}}\right] \times N_I\\ &= \frac{\pi}{4}a_R E_{\mathrm{RI}} N_R N_I \left(\frac{\rho_0}{\rho_a}\right)^{1/2}\frac{\Gamma(4+b_R)}{\lambda_R^{2+b_R}}.\end{aligned} \tag{A25}$$

4) EVAPORATION (NREVP)

Nrevp is given by (A14).

5) FREEZING (NGFRZ)

The equation for freezing of rainwater is also based on Wisner et al. (1972) and Bigg (1953) and is expressed as

$$\begin{aligned}\mathrm{Ngfrz}(\mathrm{m^{-3}\,s^{-1}}) &= -\int \frac{d}{dt}(dN_{\mathrm{DR}})\\ &= \int \frac{\pi B' D_R^3}{6}\{\exp[A'(T_0 - T)] - 1\} N_R \lambda_R^2 D_R \exp[-(\lambda_R D_R)]\, dD_R\\ &= 4\pi B' N_R\{\exp[A'(T_0 - T)] - 1\}\lambda_R^{-3}.\end{aligned} \tag{A26}$$

6) MELTING (NSMLT, NSEML, NGMLT, AND NGEML)

The number concentration of rainwater is also affected by the melting processes of snow and graupel. The authors of the present study assume that the melted graupel–snow number concentration is equal to the raindrop number concentration. The effect of snow melting is expressed as

$$\mathrm{Nsmlt}(\mathrm{m^{-3}\,s^{-1}}) = \frac{N_{0\mathrm{S}}}{\lambda_S q_S}(\mathrm{Psmlt}). \tag{A27}$$

Similarly, the melting of graupel affects the number concentration of rainwater and is of the following form:

$$\mathrm{Ngmlt}(\mathrm{m}^{-3}\,\mathrm{s}^{-1}) = \frac{N_{0\mathrm{G}}}{\lambda_G q_G}(\mathrm{Pgmlt}). \qquad \text{(A28)}$$

The melting of snow and graupel is enhanced by the accretion of cloud water and rain and can be expressed as

$$\mathrm{Nseml}(\mathrm{m}^{-3}\,\mathrm{s}^{-1}) = \frac{N_{0\mathrm{S}}}{\lambda_S q_S}(\mathrm{Pseml}) \qquad \text{(A29)}$$

and

$$\mathrm{Ngeml}(\mathrm{m}^{-3}\,\mathrm{s}^{-1}) = \frac{N_{0\mathrm{G}}}{\lambda_G q_G}(\mathrm{Pgeml}). \qquad \text{(A30)}$$

The accretion process of cloud water by snow and graupel is not added to the number concentration of rainwater because the effect is considered in the enhanced melting processes.

REFERENCES

Bernardet, L. R., and W. R. Cotton, 1998: Multiscale evolution of a derecho-producing mesoscale convective system. *Mon. Wea. Rev.,* **126,** 2991–3015.

Berry, E. X., and R. L. Reinhardt, 1974: An analysis of cloud drop growth by collection. Part II: Single initial distributions. *J. Atmos. Sci.,* **31,** 1825–1831.

Bigg, E. K., 1953: The supercooling of water. *Proc. Phys. Soc. London,* **B66,** 688–694.

Biggerstaff, M. I., and R. A. Houze Jr., 1991a: Kinematic and precipitation structure of the 10–11 June 1985 squall line. *Mon. Wea. Rev.,* **119,** 3034–3065.

——, and ——, 1991b: Midlevel vorticity structure of the 10–11 June 1985 squall line. *Mon. Wea. Rev.,* **119,** 3066–3079.

Cohard, J.-M., and J.-P. Pinty, 2000a: A comprehensive two-moment warm microphysical bulk scheme. I: Description and tests. *Quart. J. Roy. Meteor. Soc.,* **126,** 1815–1842.

——, and ——, 2000b: A comprehensive two-moment warm microphysical bulk scheme. II: 2D experiments with a non-hydrostatic model. *Quart. J. Roy. Meteor. Soc.,* **126,** 1815–1842.

Cotton, W. R., G. J. Tripoli, R. M. Rauber, and E. A. Mulvihill, 1986: Numerical simulation of the effects of varying ice crystal nucleation rates and aggregation processes on orographic snowfall. *J. Climate Appl. Meteor.,* **25,** 1658–1680.

Dudhia, J., 1989: Numerical study of convection observed during the winter monsoon experiment using a mesoscale two-dimensional model. *J. Atmos. Sci.,* **46,** 3077–3107.

——, S.-Y. Hong, and K.-S. Lim, 2008: A new method for representing mixed-phase particle fall speeds in bulk microphysics parameterizations. *J. Meteor. Soc. Japan,* **86A,** 33–44.

Fan, J., R. Zhang, G. Li, W.-K. Tao, and X. Li, 2007: Simulations of cumulus clouds using a spectral microphysics cloud-resolving model. *J. Geophys. Res.,* **112,** D04201, doi:10.1029/2006JD007688.

Ferrier, B. S., 1994: A double-moment multiple-phase four-class bulk ice scheme. Part I: Description. *J. Atmos. Sci.,* **51,** 249–280.

Fovell, R. G., G. L. Mullendore, and S.-H. Kim, 2006: Discrete propagation in numerically simulated nocturnal squall lines. *Mon. Wea. Rev.,* **134,** 3735–3752.

Ghan, S. J., L. R. Leung, and R. C. Easter, 1997: Prediction of cloud droplet number in a general circulation model. *J. Geophys. Res.,* **102,** 21 777–21 794.

Hong, S.-Y., and J.-O. J. Lim, 2006: The WRF single-moment 6-class microphysics scheme (WSM6). *J. Korean Meteor. Soc.,* **42,** 129–151.

——, and K.-S. S. Lim, 2009: The WRF double-moment cloud microphysics scheme (WDM). *Proc. The Third East Asia WRF Workshop and Tutorial,* Seoul, South Korea, Joint Center for High-Impact Weather and Climate Research, 14.

——, J. Dudhia, and S.-H. Chen, 2004: A revised approach to ice microphysical processes for the bulk parameterization of clouds and precipitation. *Mon. Wea. Rev.,* **132,** 103–120.

Houze, R. A., Jr., 1993: *Cloud Dynamics*. Academic Press, 573 pp.

Ikawa, M., and K. Saito, 1991: Description of a nonhydrostatic model developed at the forecast research department of the MRI. Meteorological Research Institude Tech. Rep. 28, 238 pp.

Joss, J., K. Schran, J. C. Thoms, and A. Waldvogel, 1970: On the quantitative determination of precipitation by radar. Scientific Communication 63, Research Department of the Federal Commission on the Study of Hail Formation and Hail Suppression, Ticinese Observatory of the Swiss Central Meteorological Institute, 38 pp. [Available from Swiss Federal Institute of Technology Zurich, ETH Zortrum, CH-8092 Zurich, Switzerland.]

Kessler, E., 1969: *On the Distribution and Continuity of Water Substance in Atmospheric Circulations. Meteor. Monogr.,* No. 32, Amer. Meteor. Soc., 84 pp.

Khain, A. P., N. BenMoshe, and A. Pokrovsky, 2008: Factors determining the impact of aerosols on surface precipitation from clouds: Attempt of classification. *J. Atmos. Sci.,* **65,** 1721–1748.

Khairoutdinov, M., and Y. Kogan, 2000: A new cloud physics parameterization in a large-eddy simulation model of marine stratocumulus. *Mon. Wea. Rev.,* **128,** 229–243.

Kong, F., and M. K. Yau, 1997: An explicit approach to microphysics in MC2. *Atmos.–Ocean,* **33,** 257–291.

Leary, C. A., and R. A. Houze Jr., 1979: The structure and evolution of convection in a tropical cloud cluster. *J. Atmos. Sci.,* **36,** 437–457.

Lee, G., I. Zawadzski, W. Szyrmer, D. Sempere-Torres, and R. Uijlenhoet, 2004: A general approach to double-moment normalization of drop size distributions. *J. Appl. Meteor.,* **43,** 264–281.

Li, G., Y. Wang, and R. Zhang, 2008: Implementation of a two-moment bulk microphysics scheme to the WRF model to investigate aerosol–cloud interaction. *J. Geophys. Res.,* **113,** D15211, doi:10.1029/2007JD009361.

Li, X., W.-K. Tao, A. P. Khain, J. Shimpson, and D. E. Johnson, 2009a: Sensitivity of a cloud-resolving model to bulk and explicit bin microphysical schemes. Part I: Comparisons. *J. Atmos. Sci.,* **66,** 3–21.

——, ——, ——, ——, and ——, 2009b: Sensitivity of a cloud-resolving model to bulk and explicit bin microphysical schemes. Part II: Cloud microphysics and storm dynamics interactions. *J. Atmos. Sci.,* **66,** 22–40.

Lin, Y.-L., R. D. Farley, and H. D. Orville, 1983: Bulk parameterization of the snow field in a cloud model. *J. Climate Appl. Meteor.,* **22,** 1065–1092.

Locatelli, J. D., and P. V. Hobbs, 1974: Fall speeds and masses of solid precipitation particles. *J. Geophys. Res.,* **79,** 2185–2197.

Luo, Y., K.-M. Xu, H. Morrison, and G. McFarquhar, 2008: Arctic mixed-phase clouds simulated by a cloud-resolving model: Comparison with ARM observations and sensitivity to microphysics parameterizations. *J. Atmos. Sci.,* **65,** 1285–1303.

Martin, G. M., D. W. Johnson, and A. Spice, 1994: The measurement and parameterization of effective radius of droplets in warm stratocumulus clouds. *J. Atmos. Sci.,* **51,** 1823–1842.

Meyers, M. P., R. L. Walko, J. Y. Harrington, and W. R. Cotton, 1997: New RAMS cloud microphysics parameterization. Part II: The two-moment scheme. *Atmos. Res.,* **45,** 3–39.

Morrison, H., and J. O. Pinto, 2005: Mesoscale modeling of springtime arctic mixed phase clouds using a new two-moment bulk microphpysics scheme. *J. Atmos. Sci.,* **62,** 3683–3704.

——, J. A. Curry, and V. I. Khvorostyanov, 2005: A new double-moment microphysics parameterization for application in cloud and climate models. Part I: Description. *J. Atmos. Sci.,* **62,** 1665–1677.

——, G. Thompson, and V. Tatarskii, 2009: Impact of cloud microphysics on the development of trailing stratiform precipitation in a simulated squall line: Comparison of one- and two-moment schemes. *Mon. Wea. Rev.,* **137,** 991–1007.

Milbrandt, J. A., and M. K. Yau, 2005: A multimoment bulk microphysics parameterization. Part I: Analysis of the role of the spectral shape parameter. *J. Atmos. Sci.,* **62,** 3051–3064.

Murakami, M., 1990: Numerical modeling of dynamical and microphysical evolution of an isolated convective cloud. *J. Meteor. Soc. Japan,* **68,** 107–128.

Nagarajan, B., M. K. Yau, and D.-L. Spengler, 2004: A numerical study of a mesoscale convective system during TOGA COARE. Part II: Organization. *Mon. Wea. Rev.,* **132,** 1000–1017.

Phillips, V. T. J., L. J. Donner, and S. T. Garner, 2007: Nucleation processes in deep convection simulated by a cloud-system-resolving model with double-moment bulk microphysics. *J. Atmos. Sci.,* **64,** 738–761.

Ramanathan, V., P. J. Crutzen, J. T. Kiehl, and D. Rosenfeld, 2001: Aerosols, climate, and the hydrological cycle. *Science,* **294,** 2119–2124.

Reisner, J., R. M. Rasmussen, and R. T. Bruintjes, 1998: Explicit forecasting of supercooled liquid water in winter storms using the MM5 mesoscale model. *Quart. J. Roy. Meteor. Soc.,* **124,** 1071–1107.

Roux, F., 1988: The West African squall line observed on 23 June 1981 during COPT 81: Kinematics and thermodynamics of the convective region. *J. Atmos. Sci.,* **45,** 406–426.

Rutledge, S. A., and P. V. Hobbs, 1983: The mesoscale and microscale structure and organization of clouds and precipitation in midlatitude cyclones. Part VIII: A model for the "seeder feeder" process in warm-frontal rainbands. *J. Atmos. Sci.,* **40,** 1185–1206.

——, and D. R. MacGorman, 1990: Positive cloud-to-ground lightning in mesoscale convective systems. *J. Atmos. Sci.,* **47,** 2085–2100.

Seifert, A., and K. D. Beheng, 2001: A double-moment parameterization for simulating autoconversion, accretion, and selfcollection. *Atmos. Res.,* **59,** 265–281.

——, and ——, 2006: A two-moment cloud microphysics parameterization for mixed-phase clouds. Part II: Maritime vs. continental deep convective storms. *Meteor. Atmos. Phys.,* **92,** 67–82.

Shi, J. J., W.-K. Tao, S. Lang, S. S. Chen, C. Peters-Lidard, and S.-Y. Hong, 2007: An improved bulk microphysical scheme for studying precipitation processes: Comparisons with other schemes. *Proc. 2007 AGU Joint Assembly,* Acapulco, Mexico, Amer. Geophys. Union, A41D–02.

Skamarock, W. C., and Coauthors, 2008: A description of the advanced research WRF version 3. NCAR Tech. Note NCAR/TN-475+STR, 113 pp.

Skofronick-Jackson, G. M., J. R. Wang, G. M. Heymsfield, R. E. Hood, W. Manning, R. Meneghini, and J. A. Weinman, 2003: Combined radiometer–radar microphysical profile estimations with emphasis on high-frequency brightness temperature observations. *J. Appl. Meteor.,* **42,** 476–487.

Srivastava, R. C., 1978: Parameterization of raindrop size distributions. *J. Atmos. Sci.,* **35,** 108–117.

Tao, W.-K., and J. S. Simpson, 1993: Goddard cumulus ensemble model. Part I: Model description. *Terr. Atmos. Ocean. Sci.,* **4,** 35–72.

Thompson, G., R. M. Rasmussen, and K. Manning, 2004: Explicit forecasts of winter precipitation using an improved bulk microphysics scheme. Part I: Description and sensitivity analysis. *Mon. Wea. Rev.,* **132,** 519–542.

——, P. R. Field, R. M. Rasmussen, and W. D. Hall, 2008: Explicit forecasts of winter precipitation using an improved bulk microphysics scheme. Part II: Implementation of a new snow parameterization. *Mon. Wea. Rev.,* **136,** 5095–5115.

Tokay, A., and D. A. Short, 1996: Evidence from tropical raindrop spectra of the origin of rain from stratiform versus convective clouds. *J. Appl. Meteor.,* **35,** 355–371.

Tripoli, G. J., and W. R. Cotton, 1980: A numerical investigation of several factors contributing to the observed variable intensity of deep convection over South Florida. *J. Appl. Meteor.,* **19,** 1037–1063.

Twomey, S., 1959: The nuclei of natural cloud formation: The supersaturation in natural clouds and the variation of cloud droplet concentrations. *Pure Appl. Geophys.,* **43,** 243–249.

Waldvogel, A., 1974: The N_O jump of raindrop spectra. *J. Atmos. Sci.,* **31,** 1067–1077.

Walko, R. L., W. R. Cotton, M. P. Meyers, and J. Y. Harrington, 1995: New RAMS cloud microphysics parameterization. Part I: The single-moment scheme. *Atmos. Res.,* **38,** 29–62.

Wang, C., 2005: A modeling study of the response of tropical deep convection to the increase of cloud condensation nuclei concentration: 1. Dynamics and microphysics. *J. Geophys. Res.,* **110,** D21211, doi:10.1029/2004JD005720.

——, and J. Chang, 1993: A three-dimensional numerical model of cloud dynamics, microphysics, and chemistry 1. Concepts and formulation. *J. Geophys. Res.,* **98,** 14 827–14 844.

Wisner, C., H. D. Orville, and C. Myers, 1972: A numerical model of a hail-bearing cloud. *J. Atmos. Sci.,* **29,** 1160–1181.

Yum, S. S., and J. G. Hudson, 2002: Maritime/continental microphysical contrasts in stratus. *Tellus,* **54B,** 61–73.

Ziegler, C. L., 1985: Retrieval of thermal and microphysical variables in observed convective storms. Part I: Model development and preliminary testing. *J. Atmos. Sci.,* **42,** 1487–1509.

Zipser, E. J., 1977: Mesoscale and convective-scale downdrafts as distinct components of squall-line structure. *Mon. Wea. Rev.,* **105,** 1568–1589.